



Current strain accumulation in the hinterland of the northwest Himalaya constrained by landscape analyses, basin-wide denudation rates, and low temperature thermochronology

Kristin D. Morell^{a,*}, Mike Sandiford^b, Barry Kohn^b, Alexandru Codilean^c, Réka-H. Fülöp^{c,d}, Talat Ahmad^e

^a School of Earth and Ocean Sciences, University of Victoria, Victoria, British Columbia V8P 5C2, Canada

^b School of Earth Sciences, University of Melbourne, Parkville, Victoria 3010 Australia

^c School of Earth and Environmental Sciences, University of Wollongong, Wollongong, New South Wales 2522, Australia

^d Australian Nuclear Science and Technology Organisation (ANSTO), Lucas Heights, New South Wales 2234, Australia

^e Department of Geology, Jamia Millia Islamia University, New Delhi, India

ARTICLE INFO

Keywords:

Himalayan tectonics
Seismic cycle
Tectonic geomorphology
Erosion rates
Low temperature thermochronology

ABSTRACT

Rupture associated with the 25 April 2015 M_w 7.8 Gorkha (Nepal) earthquake highlighted our incomplete understanding of the structural architecture and seismic cycle processes that lead to Himalayan mountain building in Central Nepal. In this paper we investigate the style and kinematics of active mountain building in the Himalayan hinterland of Northwest India, approximately 400 km to the west of the hypocenter of the Nepal earthquake, via a combination of landscape metrics and long- (Ma) and short-term (ka) erosion rate estimates (from low temperature thermochronometry and basin-wide denudation rate estimates from ^{10}Be concentrations). We focus our analysis on the area straddling the PT₂, the physiographic transition between the Lesser and High Himalaya that has yielded important insights into the nature of hinterland deformation across much of the Himalaya. Our results from Northwest India reveal a distinctive PT₂ that separates a Lesser Himalaya region with moderate relief (~ 1000 m) and relatively slow erosion (< 1 mm/yr) from a High Himalaya with extreme relief (~ 2500 m), steep channels, and erosion rates that approach or exceed 1 mm/yr. The close spatial similarity in relative rates of long- and short-term erosion suggests that the gradient in rock uplift rates inferred from the landscape metrics across the PT₂ has persisted in the same relative position since at least the past 1.5 Ma. We interpret these observations to suggest that strain accumulation in this hinterland region throughout at least the past 1.5 Ma has been accomplished both by crustal thickening via duplexing and overthrusting along transient emergent faults. Despite the > 400 km distance between them, similar spatiotemporal patterns of erosion and deformation observed in Northwest India and Central Nepal suggest both regions experience similar styles of active strain accumulation and both are susceptible to large seismic events.

1. Introduction

The recent 25 April 2015 M_w 7.8 Gorkha (Nepal) earthquake underscored the seismic potential of active faults located more than 100 km from the front of the Himalayan wedge and highlighted our incomplete understanding of how strain is accumulating in the hinterland of the Himalaya (Fig. 1A and B) (Wang and Fialko, 2015; Denolle et al., 2015; Galetzka et al., 2015; Elliott et al., 2016; Whipple et al., 2016). The Nepal earthquake, and decades of seismicity records, show that moderate (M_w 5–7) to large ($M_w > 7$) earthquakes in the hinterland of the Himalaya do not always rupture to the surface and may not be

obviously related to emergent faults with conspicuous surface traces such as the Main Central Thrust (Fig. 1C, MCT) (Ni and Barazangi, 1984; Pandey et al., 1999; Denolle et al., 2015; Avouac et al., 2015). Paleoseismic trenching and/or structural field studies, which are useful in constraining fault slip histories and kinematics of the fault systems at the front of the Himalayan Range (e.g. Wesnousky et al., 1999; Kumar et al., 2001; Rajendran et al., 2015; Bollinger et al., 2014), therefore cannot be used to identify Quaternary earthquakes and the behavior of the faults that may have hosted them in the hinterland of the Himalaya.

Despite these challenges, the use of geomorphology as a proxy for rock uplift rates in the rapidly eroding and incising Himalayas, has

* Corresponding author.

E-mail address: kmorell@uvic.ca (K.D. Morell).

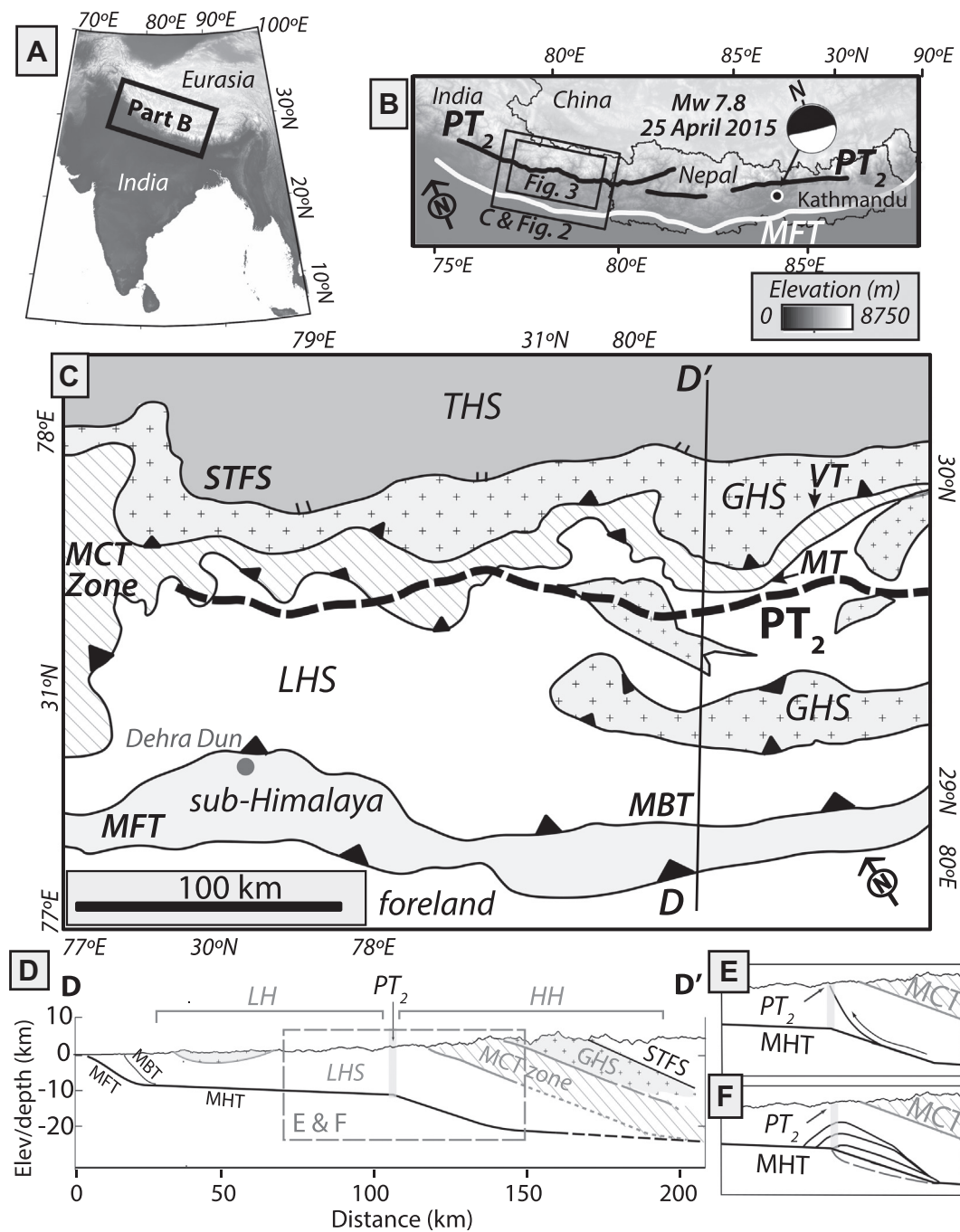


Fig. 1. A. Regional setting of the Himalaya. B. Digital elevation model with location of study area. Location of 25 April 2015 M_w 7.8 Gorkha (Nepal) earthquake and focal mechanism from Avouac et al. (2015). Approximate position of the PT_2 (physiographic transition-2) and Main Frontal Thrust (MFT) shown from Central Nepal to Northwest India (Wobus et al., 2006a; Harvey et al., 2015; Morell et al., 2015). C. Simplified geologic map (Valdiya, 1980; Srivastava and Mitra, 1994; Célérier et al., 2009a; Webb et al., 2011). GHS, Greater Himalayan Sequence; LHS, Lesser Himalayan Sequence; MBT, Main Boundary Thrust; MCT, Main Central Thrust; MT, Mansiari Thrust; STFS, South Tibetan Fault System; THS, Tethyan Himalayan Sequence; VT, Vaikrita Thrust. D. Cross section with geometry and depth of the Main Himalayan Thrust (MHT) based on receiver function analyses by Caldwell et al. (2013) and showing overthrusting model (after Cattin and Avouac, 2000). HH, High Himalaya; LH, Lesser Himalaya. E. Emergent fault model (after Wobus et al., 2006a). F. Blind duplex model (after Bollinger et al., 2004; Herman et al., 2010). Parts D–F are emulated after scenarios proposed for the active kinematics of Central Nepal applied to the current study area.

yielded important insights into our understanding of how strain is actively accumulating in the Himalayan hinterland (Seeber and Gornitz, 1983; Lavé and Avouac, 2000, 2001; Wobus et al., 2003). In particular, the presence of a physiographic transition at the base of the High Himalaya in Nepal, where prominent northward increases in relief, topography, and erosion are evident, has triggered an intense debate over the kinematics of Himalayan mountain building and its potential relationship to climate (Fig. 1B) (Seeber and Gornitz, 1983; Hodges et al., 2004; Wobus et al., 2005; Bollinger et al., 2004; Herman et al., 2010;

Godard et al., 2014). Previous studies have argued about whether this physiographic transition in Central Nepal, often referred to as the physiographic transition-2 or PT_2 (Hodges et al., 2001), is a manifestation of variations in vertical rock uplift rate due to passive slip across a décollement ramp within the mid-crust (Cattin and Avouac, 2000), a duplex that grows by underplating on the ramp (Bollinger et al., 2004; Robert et al., 2009; Herman et al., 2010), and/or an emergent fault (Wobus et al., 2006a), which may or may not be related to duplexing (Wobus et al., 2006a; Godard and Burbank, 2011). The M_w 7.8 2015

Nepal earthquake and its aftershock sequences, which ruptured at depth near the PT₂ (Fig. 1B), reignited this debate, as analyses suggest that these earthquakes confirm either overthrusting above a steep décollement ramp (Elliott et al., 2016), and/or out-of-sequence thrusting above a gently dipping décollement flat (Whipple et al., 2016).

Here we investigate the kinematics of active mountain building in the Himalayan hinterland in Northwest India, approximately 400 km to the west of the hypocenter of the 2015 Nepal earthquake (Fig. 1B). This section of the Himalaya has produced large seismic events in the past ($M_w \sim 7.7$), the last one occurring in 1803 (Rajendran and Rajendran, 2005), and exhibits a landscape morphology that is highly similar to Central Nepal. In this study, we expand upon our previous work in the region (Morell et al., 2015) by employing a series of analyses designed to evaluate the longevity of the gradients in erosion rate and rock uplift rate across the PT₂ of Northwest India (Fig. 1B) using new analyses of current landscape morphology, and both long- (Ma) and short- (ka) term estimates of erosion (from low-temperature thermochronometry and basin-wide estimates of ¹⁰Be abundances in quartz). These new analyses, and in particular the comparison of both short-term and long-term erosion rates, provide new constraints on the kinematics of the active fault systems in the hinterland region of the Himalaya that were not possible in our previous study. Our results reveal a well-defined PT₂ that separates a Lesser Himalaya region with moderate relief (~1000 m) and relatively slow rates of erosion (< 1 mm/yr) from a High Himalaya region with extreme relief (~2500 m), steep channels, and erosion rates that have approached or exceeded 1 mm/yr since at least the last 1.5 Ma. We interpret these observations to suggest that strain accumulation in this hinterland region throughout the past 1.5 Ma has been accomplished both by crustal thickening via duplexing and overthrusting along transient emergent faults.

2. Study area

2.1. Physiography, geomorphology, and climate

We focus on a ~200 km wide by ~300 km long region of Northwest India where relatively abrupt northward increases in topography, relief, and total mean annual rainfall occur across the PT₂, which lies ~100 km north of the Main Frontal Thrust (Figs. 1C and 2) (Seeber and Gornitz, 1983; Vance et al., 2003; Bookhagen and Burbank, 2006; Scherler et al., 2014; Morell et al., 2015). In this study we define the PT₂ as the southernmost extent of the steep physiography characteristic of the High Himalaya region (Hodges et al., 2001; Wobus et al., 2006a). Physiographic and climate data in the study area are shown in plan view and cross sectional view in Fig. 2. South of the PT₂, elevation remains relatively constant, between 1000 to 1500 m (Fig. 2A). From the PT₂ northwards, however, elevation progressively increases until it reaches ~5000 m at the highest peaks of the range. Relief (averaged over a ~5 km radius circle) displays a similar pattern to elevation in this region (Fig. 2B). South of the PT₂, relief is relatively constant between 1000 and 1500 m, but increases steadily at the PT₂ until it peaks at ~2500 m near the range crest. The northward increases in elevation and relief at the PT₂ also correspond with a significant increase in mean annual precipitation (Fig. 2C). South of the PT₂, precipitation for the 7-year period between January 1998 to December 2005 averages 1–1.5 m/yr (Bookhagen and Burbank, 2006). North of the PT₂, precipitation nearly doubles to 2 to 2.5 m/yr. In addition to the increases in topography and rainfall, previous studies by us (Morell et al., 2015) and others (Seeber and Gornitz, 1983; Vance et al., 2003; Scherler et al., 2014) have shown that both millennial denudation rates and river channel steepness also substantially increase northward across the PT₂ in this region (Fig. 2D). These geomorphic, erosional and topographic observations have been collectively inferred to result primarily from a northward increase in contemporary rates of rock uplift across the PT₂, rather than from the observed precipitation gradient alone (Scherler et al., 2014; Morell et al., 2015).

2.2. Bedrock geology

The region displays the classical sub-Himalayan, Lesser Himalayan, Greater Himalayan, and Tethyan Himalayan tectonostratigraphic sequences from foreland to hinterland (Fig. 1C, LHS, GHS, and THS) (Heim and Gansser, 1939; Valdiya, 1980; Srivastava and Mitra, 1994; Célérier et al., 2009a). At the front of the range, the Main Frontal Thrust and Main Boundary Thrust deform the Neogene to Quaternary Sub-Himalayan sedimentary units (Fig. 1C and D, MFT, MBT) (Valdiya, 1980; Powers et al., 1998). North of the Main Boundary Thrust, the Paleoproterozoic to Paleozoic Lesser Himalayan sequences (Fig. 1C and D, LHS), are imbricated into a duplex and overlain by several klippe comprised of Neoproterozoic through Ordovician gneiss and high-grade metamorphic rocks of the Greater Himalayan Sequence (Fig. 1C and D, GHS) (Srivastava and Mitra, 1994; Ahmad et al., 1999; Célérier et al., 2009a; Mandal et al., 2015; Mandal et al., 2016). The Main Central Thrust zone (MCT, Fig. 1C and D), a series of thrust structures separating the Lesser Himalayan from Greater Himalayan units, contains the inverted metamorphic sequence typical of many Himalayan transects (e.g. Central Nepal) in its hanging wall (Valdiya, 1980; Célérier et al., 2009a; Mandal et al., 2015). Near the peak of the range, the north-dipping South Tibetan fault system (STFS, Fig. 1C and D) separates the Greater Himalayan Sequences units to the south from the lower-grade Neoproterozoic-Eocene Tethyan Himalayan sequences to the north (Burchfiel et al., 1992). These mapped faults and lithologic contacts do not coincide with the location of the PT₂ (Fig. 1C). Each of the units in this region is relatively quartz-rich, making the study area suitable for cosmogenic erosion rate analyses that rely on estimates of ¹⁰Be concentrations in quartz (Bierman and Steig, 1996). We note that while some studies use tectonostratigraphic units to divide the Lesser and High Himalayan regions (e.g. Srivastava and Mitra, 1994; Célérier et al., 2009a), in this study we refer to the Lesser Himalaya as the region south of the PT₂, and the High Himalaya as the region north of the PT₂.

2.3. Active structures

Receiver function analyses show the active Main Himalayan Thrust décollement in this region, which has hosted seismic events with M_w 5–7 in the past (Ni and Baranzangi, 1984; Kayal et al., 2003), contains a flat beneath the Lesser Himalaya, but steepens northwards to a moderately-dipping (16°) ramp at depths between 10 and 25 km beneath the High Himalaya (Fig. 1D) (Caldwell et al., 2013). Recent studies by us (Morell et al., 2015) and others (Scherler et al., 2014) in the study area have shown that the differential rock uplift caused by the northward transition from this décollement flat to décollement ramp are responsible for the changes in geomorphology and spatial patterns of denudation rates observed across the PT₂. But, the question as to whether there are additional active faults in the High Himalaya above the décollement ramp remains less clear. On the basis of high-temperature thermochronology studies in the region (⁴⁰Ar/³⁹Ar in white mica), the thrusts that make up the Main Central Thrust zone here have been reported as inactive since the late Miocene (Célérier et al., 2009b). Other authors, however, using either seismicity (Kayal et al., 2003; Mahesh et al., 2013, 2015) or observed gradients in low-temperature thermochronologic cooling ages (Patel et al., 2007; Patel and Carter, 2009; Singh et al., 2012; Patel et al., 2015) report more recent (Plio-Quaternary) activity of several of the mapped regional thrust faults such as the Munsiari and Vaikrita Thrusts that are considered part of the Main Central Thrust zone (Fig. 1C, MT and VT). Similar to Central Nepal, the differential rock uplift inferred across the PT₂ in this region could be produced by one or a combination of the following scenarios: 1) passive overthrusting across the décollement ramp with no additional out-of-sequence deformation (Fig. 1D) (e.g. Cattin and Avouac, 2000), 2) an emergent thrust fault located at the PT₂ that is not currently mapped at the surface (Fig. 1E) (e.g. Wobus et al., 2006a; Whipple et al., 2016), and/or 3) an actively growing blind duplex on

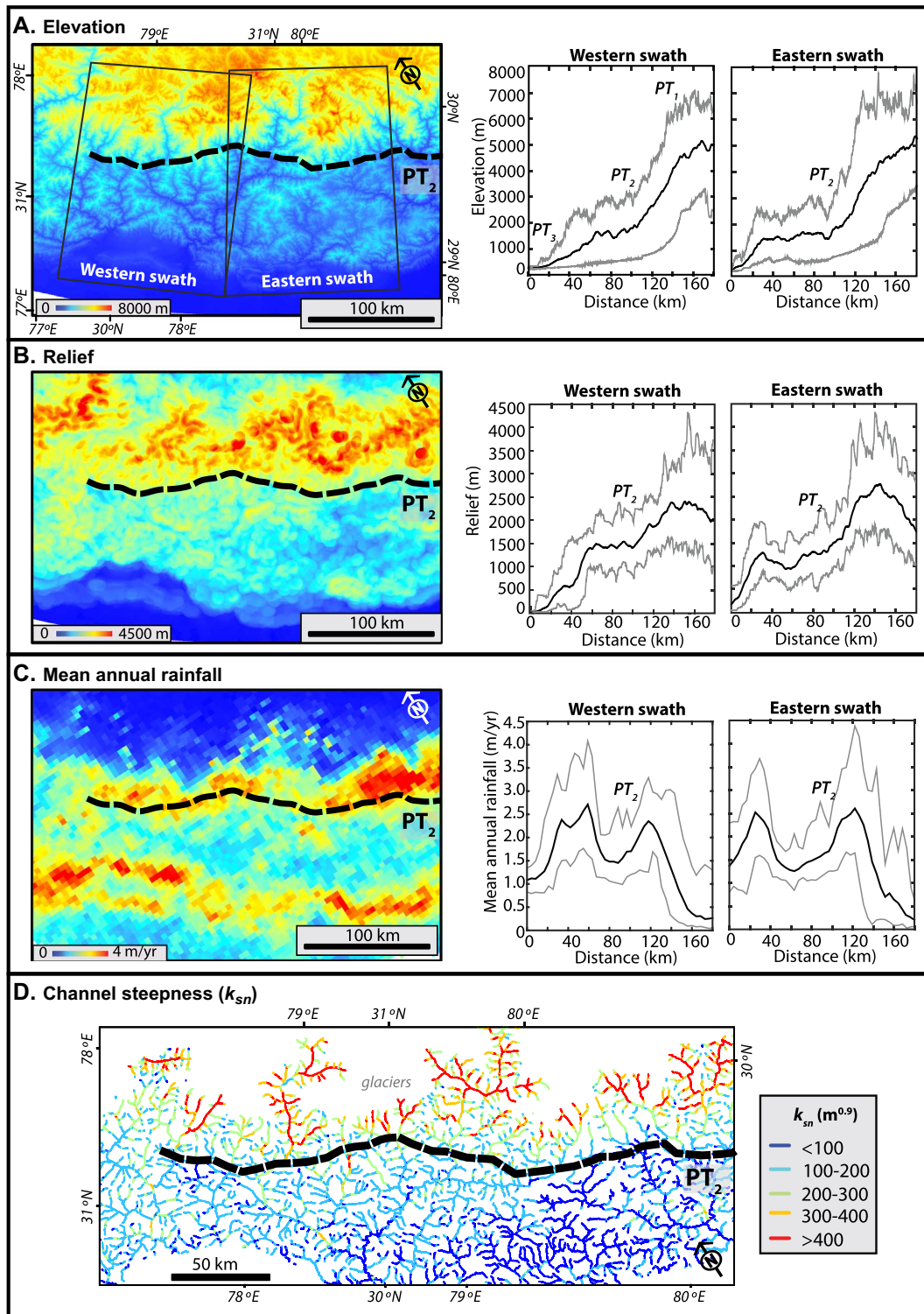


Fig. 2. A. Plan view map of elevation data (from Shuttle Radar Topography Mission ~30-m dataset; <http://www2.jpl.nasa.gov/srtm/>) for area shown on Fig. 1B. Swath profiles (~130 km wide), showing maximum, minimum and mean elevation data from western and eastern swath locations indicated by black polygons on the map. B. Relief calculated over a circle with ~5 km radius from elevation data shown in panel A with swath profiles from the same locations as part A. C. Mean annual rainfall data from Tropical Rainfall Measurement Mission (TRMM) (Bookhagen and Burbank, 2006) with swath profiles as in parts A–C. D. Normalized river channel steepness (k_{sn}) calculated using slope-area method from Morell et al. (2015). Data were calculated over 1 km-long river segments for all channels with drainage areas greater than 10 km² and $\theta_{ref} = 0.45$.

the décollement ramp (Fig. 1F) (e.g. Robert et al., 2009; Herman et al., 2010). But, the viability of these models has not been tested for the study area in Northwest India. Here we evaluate these potential kinematic models with respect to temporal and spatial variations in physiography and erosion rate, as described below.

3. Methods

In order to place constraints on the kinematics of active hinterland structures, we employ a collection of analyses designed to test for potential spatial and temporal gradients in vertical erosion rate and rock

uplift rate across the PT₂ of Northwest India. First, we estimate patterns of millennial basin-wide denudation rates across the PT₂ using new ($n = 8$) and previously published ($n = 19$) (Scherler et al., 2014; Morell et al., 2015) estimates of ¹⁰Be concentrations in quartz (Bierman and Steig, 1996), together with a series of landscape metrics that are shown to scale positively with rock uplift rate in tectonically active regions, including relief, hillslope angles and river channel steepness (k_{sn}) (Whipple and Tucker, 1999; Hurtrez et al., 1999; Willett and Brandon, 2002; Burbank et al., 2003; Lague et al., 2005; Wobus et al., 2006b; Kirby and Whipple, 2012). Second, for those areas without basin-wide denudation rates from ¹⁰Be, we use the well-established relationships between k_{sn} and basin-wide denudation rate to map predicted rates of basin-wide millennial denudation across the landscape (Ouimet et al., 2009; Cyr et al., 2010; DiBiase and Whipple, 2011; Kirby and Whipple, 2012; Forte et al., 2016). These new landscape and denudation rate analyses improve upon our previous work in the region (Morell et al., 2015) by providing a more comprehensive erosion rate and landscape metric dataset than was presented in our previous study. Third, to test for the longevity of the millennial landscape and erosion rate patterns, and their implications for the kinematics of active mountain building over time scales that span millions of years, we compare the results from our landscape analysis and millennial denudation rates with new and previously published estimates of longer-term exhumation from three low-temperature thermochronometric systems (zircon (U-Th)/He, apatite fission track and apatite (U-Th-Sm)/He). Finally, we place these new constraints on relative rates of vertical rock uplift and erosion in the context of active strain accumulation by comparing our datasets with published seismicity data (Mahesh et al., 2013, 2015), the geophysically-determined décollement geometry beneath the Himalayan wedge (Caldwell et al., 2013), and global navigation satellite system (GNSS) signals (Jade et al., 2014; Stevens and Avouac, 2015).

3.1. Basin-wide averaged denudation rate estimates from ¹⁰Be concentrations in quartz

We calculated basin-wide averaged denudation rates from fluvial sand samples using measurements of the concentration of beryllium-10 (¹⁰Be) in quartz. The ¹⁰Be radionuclide is produced *in situ* by high-energy cosmic radiation breaking up the atoms that make up the minerals and rocks at the earth's surface. The application of ¹⁰Be to the study of earth surface processes is based on the principle that its concentration is directly proportional to the exposure time to cosmic radiation. ¹⁰Be accumulates in surficial deposits over time such that its concentration is directly related to not only the exposure age but also the rate at which the surface is eroding (Lal, 1991). Assuming that the collected sediment is a well-mixed representative of upstream areas, this technique provides denudation rate estimates averaged spatially over the sampled basin and averaged temporally over the time it takes to erode ~60 cm of rock from the surface, which is commonly 10²–10⁵ years (Bierman and Steig, 1996; Granger et al., 1996; von Blanckenburg, 2005). To date, ¹⁰Be-based denudation rates have been determined in more than two thousand river basins worldwide, and these analyses have contributed substantially to our understanding of the relative effects of climate, topography and tectonics on denudation rates in a wide range of tectonic settings (Portenga and Bierman, 2011; Willenbring et al., 2013).

We collected eight new samples within active fluvial channels at the outlet of relatively small (~5–75 km²) tributaries. In order to exclude the effects of sediment storage and to ensure that the samples were representative of the upstream drainage area, samples were collected from the active channel, away from point bars, fluvial terraces or recent landslides. The tributaries sampled were chosen to be large enough to decrease the effects of landslides on the ¹⁰Be inventory of the sample (Niemi et al., 2005), but small enough to evaluate potential spatial patterns in erosion rate. We avoided main stem channels because of active glaciation in their headwaters, and because of the common

presence of thick alluvial fills (Srivastava et al., 2008; Ray and Srivastava, 2010; Godard et al., 2012; Scherler et al., 2015).

Quartz was separated and cleaned following procedures based on Kohl and Nishiizumi (1992) using froth flotation to separate feldspars from quartz, and ¹⁰Be was extracted using ion chromatography following procedures described in von Blanckenburg et al. (1996). The ¹⁰Be/⁹Be ratios were measured on the ANTARES 10 MV tandem accelerator at the Australian Nuclear Science and Technology Organisation (ANSTO) (Fink and Smith, 2007), and were normalized to the 2007 KNSTD standard KN01-5-2 with a nominal ¹⁰Be/⁹Be ratio of 8.558×10^{-12} (Nishiizumi et al., 2007). Errors for the final ¹⁰Be concentrations (atoms g⁻¹) for all samples were calculated by summing in quadrature the statistical error for the AMS measurement, 2% for reproducibility, and 1% for uncertainty in the Be spike concentration. Blank corrected ¹⁰Be/⁹Be ratios ranged between $43.47 \pm 2.59 \times 10^{-15}$ and $234.84 \pm 6.67 \times 10^{-15}$. Analytical errors ranged from 3.6 to 7.9%.

We synthesized our new data together with other similar denudation rate analyses reported previously in the study area (Scherler et al., 2014; Morell et al., 2015), but excluded basins from these studies that contained active glaciers or significant snow cover due to potential shielding affects. We also excluded data that appeared to be significant outliers by comparison with other regional trends. For consistency, but also to allow for easy comparisons of denudation rates with other basins worldwide, we performed calculations following Willenbring et al. (2013). To this end, we calculated denudation rates using the formalism of Schaller et al. (2001) with ¹⁰Be sea-level, high-latitude (SLHL) production rates of 4.5 ± 0.5 atoms g⁻¹ yr⁻¹ for high-energy neutrons, 0.097 ± 0.007 atoms g⁻¹ yr⁻¹ for slow muons, and 0.085 ± 0.012 atoms g⁻¹ yr⁻¹ for fast muons. We recalculated the ¹⁰Be SLHL production rate for high-energy neutrons from Balco et al.'s (2008) ¹⁰Be calibration-site dataset, using the time-independent altitude/latitude scaling scheme of Dunai (2000) and the updated ¹⁰Be half-life of 1.387 ± 0.012 Ma (Chmeleff et al., 2010; Korschinek et al., 2010). We used the ¹⁰Be production rates for muons provided in Kubik et al. (2009) and based on Heisinger et al. (2002a,b). We corrected all ¹⁰Be SLHL production rates for altitude and latitude using the time-independent scaling scheme of Dunai (2000) and for topographic shielding following Codilean (2006).

3.2. Landscape metrics

3.2.1. Basin-wide relief, hillslope and precipitation

We calculated mean basin-wide relief, hillslope angles and annual precipitation for select catchments within the study area, so that each of these landscape metrics can be directly compared with the basin-averaged ¹⁰Be denudation rate data. In this analysis, we hand-selected glacier-free tributary basins that were greater than ~10 km² but less than ~100 km² in area using accumulation grids based on NASA's 1-arc-second (~30 m) Shuttle Radar Topography Mission (SRTM) dataset (<http://www2.jpl.nasa.gov/srtm/>). We chose this basin size so that the catchments were small enough that they do not cross differences in tectonic, climatic or glacial regimes but large enough that they allow for the river network to be well-developed. Basin relief was calculated for each basin by subtraction of the highest and lowest elevations within each watershed (see Ouimet et al., 2009), with uncertainties on basin relief fixed at the standard precision of the SRTM dataset (~20 m) (Falorni et al., 2005). Calculation of relief using this method ensures that no data outside of the basin are used in the relief calculation, as would occur if the relief calculated over a ~5 km radius circle (i.e. Fig. 2B) were clipped to individual watersheds. Basin-wide hill-slope angles were estimated using a standard 3 × 3 neighborhood pixel-by-pixel calculation of the SRTM DEM clipped to each watershed. In order to evaluate the potential effects of precipitation on denudation rates, we also computed catchment-wide annual precipitation estimates for each of the basins analyzed in this study (using ~4-km-resolution

Tropical Rainfall Measurement Mission (TRMM) data from Bookhagen and Burbank (2006).

3.2.2. Channel steepness

Decades of research have shown that for landscapes that are in topographic steady state, rock uplift rates scale with river channel steepness, if the influences of climate and lithology are taken into account (Snyder et al., 2000; Wobus et al., 2003; Wobus et al., 2006b; Kirby and Whipple, 2012). The normalized channel steepness index, or k_{sn} , derives from a variation of Hack's law (Hack, 1957; Flint, 1974), which describes the shape of a graded river profile in terms of local slope (S), concavity (θ) and contributing area (A) according to the following power law relationship:

$$S = k_{sn} A^{-\theta_{ref}} \quad (1)$$

The use of a fixed reference concavity (θ_{ref}) in this equation allows an estimation of river channel steepness that is normalized to variations in basin shape and contributing drainage area (Wobus et al., 2006b; Kirby and Whipple, 2012).

The most widely used method for estimating k_{sn} relies on a regression in log-log space of S versus A extracted from a DEM (slope-area method) (Wobus et al., 2006b), as was used in our previous analysis in the region (Fig. 2D) (Morell et al., 2015). Here we calculate basin-wide k_{sn} using an alternative method described by Perron and Royden (2013), by estimation of the slope of the best-fit line on a plot of elevation versus an integral quantity χ , which represents a horizontal transformation of the river profile (integral method) (Harkins et al., 2007). In our calculations of basin-wide k_{sn} using this integral method, we used the common reference concavity of 0.45, so that the k_{sn} data can be compared to similar global datasets (see Kirby and Whipple, 2012).

We used the integral method in our analysis for several reasons. First, the integral method allows ready calculation of basin-wide k_{sn} , which makes calculation of predicted denudation rate using the established relationships between basin-wide k_{sn} and basin-wide denudation rate relatively straightforward (e.g. Ouimet et al., 2009; Forte et al., 2016). In this region, k_{sn} calculations using the slope-area method require smoothing of elevation data over a 10-km window in order to sufficiently remove noise in the DEM (Wobus et al., 2006b; Morell et al., 2015). This relatively large smoothing window makes calculation of basin-wide averaged k_{sn} difficult for basins that are smaller or close to the size of the smoothing window (< 15 km in length), such as many of those basins for which there are basin-wide ^{10}Be -derived denudation rate data. Because the integral method does not require smoothing of the elevation data, it allows ready calculation of basin-wide-averaged k_{sn} , even for relatively short tributary basins. Second, drainage basins in equilibrium, without knickpoints and with uniform lithology should display a linear elevation- χ relationship (Perron and Royden, 2013). Therefore the goodness of fit of the elevation- χ regression line (R^2) allows a test of the steady state assumption (where $R^2 = 1$ is in equilibrium) and the identification of any knickpoints within the analyzed basin. Finally, the integral method provides an estimation of uncertainties on basin-wide k_{sn} values that can be extrapolated directly from the standard error on the elevation- χ regression.

Using the ~30-m SRTM data, Matlab™ and TopoToolbox (Schwanghart and Scherler, 2014) we calculated basin-wide k_{sn} using the integral method for hand-selected watersheds with drainage areas ~10–100 km². In order to exclude basins that were not in equilibrium with background rock uplift rates, we then excluded those basins with R^2 values < 0.6 in the elevation- χ fit. Using these selected basins, we performed least squares fits to calculate power law and linear relationships between basin-wide ^{10}Be denudation rate data and basin-wide k_{sn} data. The resultant relationship between ^{10}Be -derived denudation rate and basin-wide k_{sn} was then used to map predicted basin-wide denudation rates across the study area using the basin-wide k_{sn} data. To further confirm a landscape response to rock uplift rates, we

also explored the potential relationship between predicted basin-wide denudation rate and catchment-wide relief, hillslope angles and yearly precipitation.

3.3. Low-temperature thermochronology

To test for the longevity of the spatial patterns from our landscape and millennial denudation rate analyses, we estimated longer-term rates of exhumation based on new cooling ages from bedrock samples from three low temperature thermochronologic systems: zircon (U-Th)/He (ZHe, $n = 6$), apatite fission track (AFT, $n = 3$) and apatite (U-Th-Sm)/He (AHe, $n = 7$). Because these systems reveal information about the timing of cooling through a specific temperature sensitivity window for each system, termed the partial retention zone (ZHe: ~130–200 °C; AFT: ~60–120 °C; AHe: ~40–80 °C (Gleadow et al., 2002; Farley, 2002; Reiners et al., 2004)), they provide data for constraining the timing and rate of cooling of rocks within the upper few kilometers of the crust and indirectly their exhumation history.

Although we collected dozens of samples, only a fraction of the collected samples contained minerals suitable for dating. We therefore supplemented our dataset with ZHe cooling ages of detrital zircon grains extracted from fluvial sand samples collected at the mouths of three tributaries used in analyses in Morell et al. (2015). We further combined our new AFT age data with ~65 AFT data from previous studies, collected in the study area within ~50 km of the PT₂ and south of the mapped location of the South Tibetan fault system (Fig. 1C, STFS) (Sorkhabi et al., 1996; Patel et al., 2007; Patel and Carter, 2009; Thiede et al., 2009; Singh et al., 2012; Patel et al., 2015). We excluded any previously published data if the age uncertainty was >50% of the mean age, or if the age varied from neighboring ages by an order of magnitude or more. We calculated weighted mean ages using single grain ZHe and AHe data, but excluded single grain data that showed significant intra-sample age dispersion.

Most methods that use cooling ages to estimate exhumation rate reflect a time-averaged rate of erosion and constant cooling since each sample was last at its respective closure temperature and corresponding depth beneath the surface (Dodson, 1973). In order to interpret cooling ages in terms of rates of exhumation, we used a 1D thermal model (e.g. Moore and England, 2001) based on methods in Willett and Brandon (2013) wherein the depth corresponding to the closure temperature is determined by an evolving half-space model. This half-space model allows quantification of potential perturbations of the geotherm by both upward advection of isotherms due to erosion, and the wavelength-dependent influence of topography. This 1D modeling approach neglects the potential effects of horizontal exhumation paths, but several previous studies have shown that 1D thermal models can accurately reflect exhumation rates in the Himalaya, especially in regions where erosion rates are relatively high and modeled temperatures are less than ~350 °C (Whipp et al., 2007; Robert et al., 2009; Herman et al., 2010; Thiede and Ehlers, 2013; van der Beek et al., 2016). These studies have shown that heat flow in the Himalaya at these relatively low temperatures occurs primarily vertically, and therefore 1D thermochronologic models can reliably account for most of the heat transfer within the shallow crust (Whipp et al., 2007; Thiede and Ehlers, 2013). Although we use three thermochronological systems in this study, the spatial coverage of our data do not lend themselves to a robust joint inversion across several systems (e.g. Thiede and Ehlers, 2013; Adams et al., 2015). Our 1D approach is instead designed to compare the relative differences in exhumation rate across the PT₂ via each system independently, and to compare longer term rates of exhumation from thermochronology to shorter term rates of basin-wide denudation rate determined from ^{10}Be concentrations.

In the calculation of AFT and AHe exhumation rates, we used weighted mean ages but excluded those samples that exhibited uncertainties greater than 50% of the weighted mean age. For AFT exhumation rates, we used either pooled or central ages, depending on the

source of the published data. We calculated exhumation rates using these ages and the following parameters: 1) an onset of exhumation beginning at 20 Ma; 2) a surface temperature of 5 °C; 3) a mean elevation for each sample averaged over a 2.5 km radius circle; and 4) a present-day geothermal gradient between 35 and 45 °C/km. We chose this relatively high geothermal gradient given that many of the samples exhibit young cooling ages ($< 1\text{--}2$ Ma) and no model solutions were attainable in many instances with lower gradients. Furthermore, if cooling in this region is in fact a reflection of erosion, as has been reported across much of the Himalayan Range (e.g. Thiede and Ehlers, 2013), such young cooling ages imply rapid erosion rates, which can cause upward migration of isotherms and an increase in the geothermal gradient (Reiners and Brandon, 2006). We used these methods to create exhumation envelopes for each cooling age, based both on our imposed variations in the modern geothermal gradient and in the analytical uncertainty associated with each cooling age.

4. Results

4.1. Results from basin-wide ^{10}Be -derived denudation rate analysis

The basin-wide ^{10}Be -derived denudation rates show a pronounced northward increase across the PT₂ over millennial time scales, but remain relatively invariant along strike (Tables 1 and 2; Figs. 3A and 4A) (Scherler et al., 2014; Morell et al., 2015). ^{10}Be -derived denudation rates average ~ 0.2 mm/yr (0.16 ± 0.07 mm/yr at 1σ) for those samples whose catchment area is entirely south of the PT₂ ($n = 12$), whereas the average denudation rate for samples with drainage areas entirely north of PT₂ ($n = 4$) is approximately three times higher (mean of 0.59 ± 0.16 mm/yr). For those samples whose drainage areas cross the PT₂, encompassing areas in both the Lesser and High Himalaya ($n = 10$), denudation rates are intermediate (0.37 ± 0.13 mm/yr) between the high denudation rates in the High Himalaya and lower denudation rates in the Lesser Himalaya. Linear regressions of the ^{10}Be -denudation rate data versus distance across strike show that the data are not well-fit by a linear trend across the PT₂ (root mean square error (RMS) = 0.14). Instead, the denudation rates are better fit by relatively constant values in the Lesser Himalaya region south of the PT₂ (RMS = 0.08), and a progressive linear increase in denudation rates north of the PT₂ (RMS = 0.09) (Fig. 4A). As all of the analyzed denudation rates range between 0.05 ± 0.01 mm/yr (sample 21, Table 2) to 0.78 ± 0.18 mm/yr (sample 17, Table 2), they thus correspond to time periods between $\sim 500\text{--}10,000$ years.

4.2. Landscape metrics and predicted millennial erosion rates

Basin-wide predicted denudation rates and basin-wide k_{sn} from 545 selected basins show northward increases across the PT₂, similar to the ^{10}Be -derived denudation rate data (Figs. 4B, C and 5; Table 3). The mean predicted denudation rate south of the PT₂ is $\sim 0.1\text{--}0.2$ mm/yr, which corresponds to k_{sn} values between ~ 120 to ~ 150 m^{0.9} (Fig. 4B and C). Predicted denudation rates increase to ~ 0.3 mm/yr at the PT₂ (k_{sn} of ~ 200 m^{0.9}) and continue to increase toward the hinterland until they reach ~ 1 mm/yr (k_{sn} of $\sim 300\text{--}400$ m^{0.9}) near the peaks of the range in the High Himalaya (Figs. 4B, C and 5). Similar to the ^{10}Be data, forced regressions through both the k_{sn} (Fig. 4B) and predicted denudation rate data (Fig. 4C) show that rather than a steady linear increase across-strike of the PT₂ (k_{sn} RMS = 27.12; D_{pred} RMS = 0.11), both datasets are better fit by near-constant values south of the PT₂ (k_{sn} RMS = 8.39; D_{pred} RMS = 0.01), and a linear increase north of the PT₂ (k_{sn} RMS = 4.54; D_{pred} RMS = 0.02) (Fig. 4B and C). In our estimations of predicted basin-wide denudation rate, we used the best-fitting power law relationship between ^{10}Be -derived erosion rate and k_{sn} ($R^2 = 0.60$; Fig. 6A), but we note that a linear-least squares fit applies almost equally well ($R^2 = 0.57$) and would likely yield similar results.

For a number of reasons, the results from our landscape analyses confirm the conclusion drawn by previous studies (Scherler et al., 2015; Morell et al., 2015) that the increases in basin-wide millennial denudation rate and k_{sn} across the PT₂ reflect a northward increase in rock uplift rate. One, only a handful of basins ($n \sim 10$) were excluded from our analysis due to low R^2 values in the elevation- χ fit. This result implies an absence of knickpoints in the large majority of the analyzed basins and a condition of steady state for each of the relatively small (10–100 km² area) basins analyzed (Perron and Royden, 2013). Two, the poor correlation between basin-wide mean annual rainfall and either predicted denudation rate or ^{10}Be -derived denudation rate (Fig. 6D) suggests that rock uplift rate, rather than rainfall, is the primary control on denudation rates in this study area (Scherler et al., 2014). Moreover, although drainage areas range from ~ 4 to 210 km² in size (Table 3), we observe no systematic variation of ^{10}Be -derived denudation rates with catchment size that could reflect the possible effects of landsliding (e.g. Niemi et al., 2005).

Finally, we observe positive correlations between all of the landscape metrics that are expected to correlate with rock uplift rate in active tectonic settings (Safran et al., 2005; DiBiase et al., 2010; DiBiase and Whipple, 2011; Kirby and Whipple, 2012). There is a positive relationship between ^{10}Be -derived denudation rate and k_{sn} ($R^2 = 0.60$; Fig. 6A). And, there are positive correlations between basin relief and both the ^{10}Be -derived denudation rate data ($R^2 = 0.42$; $D_{10\text{Be}}$ in Fig. 6B) and the predicted denudation rate dataset ($R^2 = 0.69$; D_{pred} in Fig. 6B).

Table 1

Results of ^{10}Be analyses in river sediment samples and basin-wide denudation rate calculations.

Sample #	AMS ID	Lat. [deg N]	Long. [deg E]	$^{10}\text{Be}/^{9}\text{Be}$ ^{a, b, c} [10^{-15}]	Sample mass [g]	^{9}Be spike [mg]	^{10}Be concentration ^{c, d} [10^3 atoms g ⁻¹]	^{10}Be production rate ^e [atoms g ⁻¹ yr ⁻¹]	Denudation rate ^{c, e} [mm yr ⁻¹]
1 (IN1403)	B5912	79.015472	30.384806	59.68 ± 3.14	41.05	0.328	31.910 ± 1.822	12.14	0.31 ± 0.04
2 (IN1405)	B5913	79.085750	30.490333	73.54 ± 5.57	47.40	0.329	34.111 ± 2.693	18.21	0.41 ± 0.05
3 (IN1408)	B5914	78.996980	30.623170	106.88 ± 5.79	40.34	0.330	58.403 ± 3.422	25.73	0.32 ± 0.04
4 (IN1409)	B5915	79.012867	30.611083	110.62 ± 5.54	38.46	0.329	63.280 ± 3.470	23.68	0.28 ± 0.03
5 (IN1410)	B5916	79.020083	30.594350	57.21 ± 3.94	40.47	0.330	31.190 ± 2.257	19.70	0.48 ± 0.06
6 (IN1401)	B5972	78.861722	30.238444	43.47 ± 2.59	29.80	0.330	32.206 ± 2.049	9.92	0.26 ± 0.03
7 (IN1402)	B6070	78.935194	30.258278	234.84 ± 6.67	43.30	0.273	99.068 ± 3.580	10.19	0.08 ± 0.01
8 (IN1404)	B6071	79.052500	30.407972	47.48 ± 2.00	19.39	0.271	44.401 ± 2.115	12.07	0.22 ± 0.02

^a $^{10}\text{Be}/^{9}\text{Be}$ ratios were normalized to SRM KN-5-2 (same as 07KNSTD) with a nominal ratio of 8558×10^{-15} (Nishiizumi et al., 2007).

^b Corrected using the following procedural blanks: $2.998 \pm 0.728 \times 10^{-15}$ (IN1403, 05, 08, 09, and 10), $2.142 \pm 0.412 \times 10^{-15}$ (IN1401), and $2.132 \pm 0.271 \times 10^{-15}$ (IN1402 and 04).

^c Uncertainties expressed at the 1σ level.

^d Final uncertainties include 1) AMS analytical errors (the larger of the counting statistics errors and the one standard deviation of the repeated measurements), 2) standard reproducibility (2%) and 3) errors in ^{9}Be spike concentration (1%), in quadrature.

^e See text for details on calculation procedure and constants used.

Table 2Summary of published ^{10}Be data used in this study^a.

Sample #	Source	Lat. [deg N]	Long. [deg E]	^{10}Be concentration ^b [10^3 atoms g $^{-1}$]	^{10}Be production rate ^c [atoms g $^{-1}$ yr $^{-1}$]	Denudation rate [mm yr $^{-1}$] ^{b,c}
9 (DS6-AR3)	Scherler et al. (2014)	30.721396	78.088153	74.70 ± 1.58	14.55	0.15 ± 0.02
10 (DS6-006)	Scherler et al. (2014)	30.887198	78.304767	13.69 ± 0.32	26.49	1.41 ± 0.15
11 (DS7-044)	Scherler et al. (2014)	30.872129	78.303154	47.41 ± 1.20	22.95	0.36 ± 0.04
12 (DS7-045)	Scherler et al. (2014)	30.820332	78.207377	139.03 ± 3.46	14.22	0.08 ± 0.01
13 (DS7-051)	Scherler et al. (2014)	30.721162	78.087348	49.01 ± 1.25	14.55	0.23 ± 0.02
14 (DS7-061)	Scherler et al. (2014)	30.799659	78.111413	85.24 ± 2.13	14.77	0.13 ± 0.01
15 (DS7-062)	Scherler et al. (2014)	30.990885	78.019605	66.33 ± 1.98	12.98	0.15 ± 0.02
16 (DS7-066)	Scherler et al. (2014)	31.019621	78.035421	24.56 ± 0.70	19.37	0.59 ± 0.07
17 (IN1203)	Morell et al. (2015)	30.486429	79.485861	23.711 ± 5.016	25.23	0.78 ± 0.18
18 (IN1206)	Morell et al. (2015)	30.525675	79.508668	27.796 ± 3.567	25.88	0.68 ± 0.11
19 (IN1214)	Morell et al. (2015)	30.379687	79.322587	33.799 ± 4.557	14.03	0.33 ± 0.06
20 (IN1224)	Morell et al. (2015)	30.613711	78.315200	53.237 ± 12.609	13.02	0.19 ± 0.05
21 (IN1228)	Morell et al. (2015)	30.673780	78.354840	207.57 ± 19.792	14.67	0.05 ± 0.01
22 (IN1230)	Morell et al. (2015)	30.687596	78.358238	136.357 ± 13.353	13.74	0.08 ± 0.01
23 (IN1232)	Morell et al. (2015)	30.736130	78.348407	68.447 ± 8.979	14.14	0.16 ± 0.03
24 (IN1234)	Morell et al. (2015)	30.744311	78.359512	40.843 ± 5.847	15.75	0.30 ± 0.05
25 (IN1235)	Morell et al. (2015)	30.738940	78.407613	86.127 ± 14.162	17.43	0.15 ± 0.03
26 (IN1240)	Morell et al. (2015)	30.766367	78.591135	27.089 ± 3.946	19.76	0.55 ± 0.10
27 (IN1247)	Morell et al. (2015)	30.753644	78.473932	38.871 ± 13.29	20.12	0.39 ± 0.14

^a Sample in italics excluded as outlier (sample 10), as it is nearly double the next highest erosion rate (sample 17).^b Uncertainties expressed at the 1 σ level.^c Values recalculated and therefore different from those originally published. See text for details.

There appears to be no correlation between ^{10}Be -derived denudation rate and basin-wide hillslope angles for the 26 ^{10}Be -derived denudation rate samples used in our analysis ($D_{^{10}\text{Be}}$ in Fig. 6C). But, there is a moderate correlation between predicted denudation rate and mean hillslope angles ($n = 519$; $R^2 = 0.42$; D_{pred} in Fig. 6C). These observations imply that a large spread in sampled hillslope angles is required when evaluating the potential relationships between erosion rate and hillslope angles in this type of setting. Taken together, the correlations between erosion rate, k_{sn} , relief and hillslope angles point to a landscape response to a northward increase in rock uplift rate across a sharp PT₂ throughout at least the past ~500–10,000 years, the time period encompassed by the ^{10}Be -derived denudation rates (Tables 1 and 2).

4.3. Results from low-temperature thermochronometry

Similar to the erosion rate and landscape data, the results from our low-temperature thermochronologic analyses reveal a trend of apparent age decrease northwards across the PT₂ for each of the three thermochronologic systems analyzed (Figs. 3B and 4D; Tables 4–6) and a corresponding increase in exhumation rate (Fig. 4E–G; Tables 7 and A.1).

4.3.1. Zircon (U-Th)/He

Three weighted mean ZHe ages from the High Himalaya north of the PT₂ are ~2 Ma in age, and younger than two weighted mean ZHe ages that range between ~5–10 Ma sampled from the area south of the PT₂ (Figs. 3B and 4D; Table 4). The one ZHe exhumation rate we obtained from the High Himalaya is ~3.5 mm/yr (sample 2, Table 7), which is considerably higher than the two ZHe exhumation rates in the Lesser Himalaya on the order of ~1 mm/yr (samples 3 and 5 in Table 7; Fig. 4E). These ZHe exhumation rates represent time-averaged rates of exhumation across the late Miocene to Pleistocene (9.7 ± 3.3 Ma (sample 3) to 1.8 ± 0.1 Ma (sample 2), Table 4).

The three detrital samples analyzed for ZHe from the Lesser Himalaya region generally agree with the overall trend apparent in the ZHe bedrock sample data (Table 4 and Fig. 3B). Unfortunately, single grain ages of detrital samples 7 and 8 (Table 4) show relatively wide dispersion and do not cluster around a mean age. But, each of the single ZHe grain ages in the Lesser Himalaya is nonetheless older by a significant margin than the single grain ages in the High Himalaya

(Table 4). One sample with consistent single grain ages that allowed calculation of a weighted mean age (5.2 ± 2.2 Ma, sample 9) is similar in age to the bedrock ZHe sample 5 (4.9 ± 0.6 Ma) from the Lesser Himalaya region (Fig. 3B and Table 4).

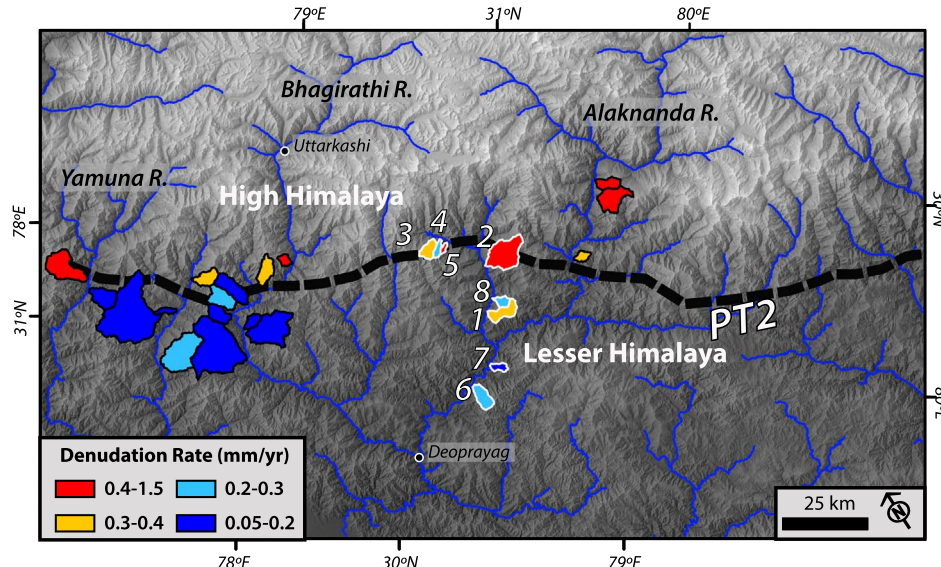
Intra-sample age dispersion in zircon bedrock samples can mainly be attributed to the effects of radiation damage on He diffusion, intracrystalline U-Th parent zonation, fluid inclusions and grain-size variation (e.g. Guenthner et al., 2013; Orme et al., 2015; Danišk et al., 2017). It is not clear which of these effects may have specifically resulted in some of the age dispersion observed, for example in bedrock sample 2 (analysis 9172) and sample 4 (Table 4). However, analysis 9456 in sample 1 (yielding an age of 1.8 ± 0.1 Ma) has been excluded from the mean weighted age calculation as it has a relatively high eU (a proxy for radiation damage), but such an age relationship is not apparent in other high eU grains such as sample 4 (analysis 9206) or sample 3 (analysis 9187) (Table 4).

4.3.2. Apatite fission track

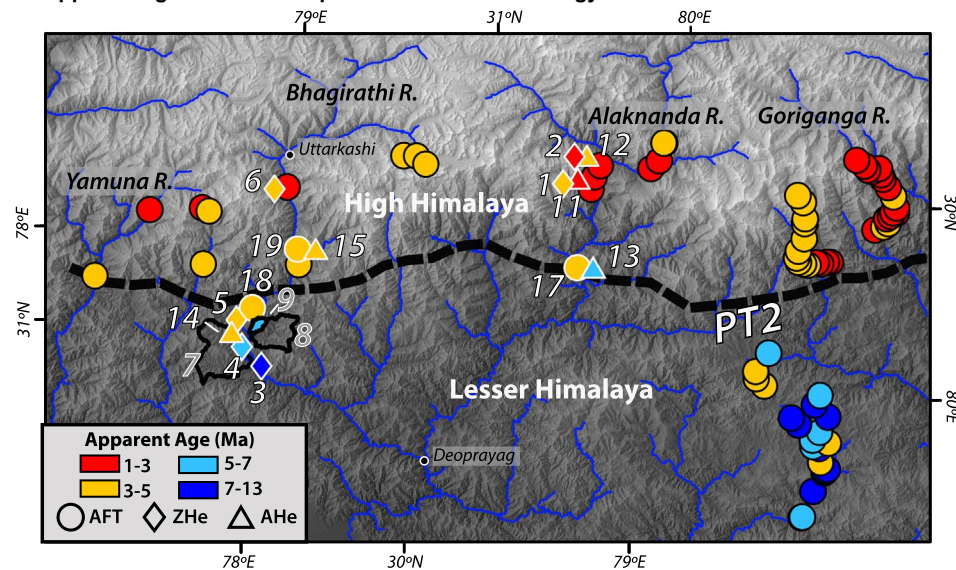
The combined AFT dataset including new ($n = 3$) and previously published data ($n = 67$) reveals a similar trend to the ZHe data across the PT₂. AFT ages are four times higher on average in the High Himalaya north of the PT₂ (mean = 2.0 ± 1.1 Ma, $n = 47$) than they are in the Lesser Himalaya to the south (mean = 8.0 ± 3.2 Ma, $n = 23$) (Figs. 3B and 4D; Tables 5 and A.1). These ages correspond to exhumation rates that are on average consistently slower in the Lesser Himalaya (less than ~1 mm/yr) than in the High Himalaya where exhumation rates average greater than ~2–3 mm/yr (Fig. 4F). Linear regressions of the entire AFT exhumation rate dataset versus distance across strike from the PT₂ are not as well fit (RMS = 0.45) as similar regressions that treat the Lesser and High Himalaya regions separately (RMS Lesser Himalaya = 0.23; RMS High Himalaya = 0.36) (Fig. 4F). These results suggest that the AFT exhumation rates do not increase linearly across-strike, rather there is an abrupt increase in AFT exhumation rates across the PT₂. Despite numerous collected samples, we were unfortunately able to obtain apatite grains suitable for AFT analyses in only three of our samples (Table 5), and able to calculate a robust exhumation rate from only one sample (sample 17, Table 7).

Our results reveal significant variability in AFT exhumation rates, particularly within the High Himalaya region (Fig. 4F). Given the relatively young apparent AFT and ZHe ages in this region (Fig. 3B;

A. Basin-wide denudation rate from ^{10}Be



B. Apparent age from low-temperature thermochronology



(Tables 4, 5 and A.1), it is likely that a large majority of this variability is related to extremely rapid cooling within the Plio-Quaternary time period, with exhumation rates in excess of at least 2–3 mm/yr. As was pointed out by Thiede and Ehlers (2013), thermochronometer data such as these have decreased sensitivity with such high exhumation rates. In fact, for the youngest AFT ages analyzed (< 0.7 Ma) no solutions to our 1D modeling were attainable with the imposed geothermal gradients of 35–45 °C/km (Table A.1). It is also possible that the variability in exhumation rate within the High Himalaya region is due to differential rock uplift caused by slip along active faults (e.g. Patel and Carter, 2009) and we explore this idea in more detail in the Discussion section of this paper. Nonetheless, the largest gradient in apparent AFT ages occurs at the PT₂, where there is at least a 2–3-fold difference in apparent AFT ages and associated exhumation rates between the Lesser and High Himalaya regions (Fig. 4D and F).

4.3.3. Apatite (U-Th-Sm)/He

Exhibiting a trend similar to the ZHe and AFT datasets, weighted mean ages from two AHe samples in the High Himalaya north of the PT₂ are on the order of ~2 Ma whereas apparent AHe ages from two

Fig. 3. A. New (white outlines) and previously published (black outlines) (Scherler et al., 2014; Morell et al., 2015) basin-wide denudation rate estimates derived from ^{10}Be concentrations in quartz from fluvial sand samples. B. Average apparent ages from zircon Helium (ZHe), apatite fission track (AFT), and apatite Helium (AHe) from bedrock samples (Sorkhabi et al., 1996; Patel et al., 2007; Patel and Carter, 2009; Thiede et al., 2009; Singh et al., 2012; Patel et al., 2015). Sample numbers from this study are shown with white outlines. The three watersheds sampled for detrital ZHe analyses are shown as black polygons, with sample number in grey.

samples close to and slightly south of the PT₂ yield weighted mean ages of ~5–6 Ma (Table 6; Figs. 3B and 4D). These apparent AHe ages correspond to exhumation rates of ~1 mm/yr in the High Himalaya north of the PT₂ and slower exhumation rates on the order of ~0.5 mm/yr at or south of the PT₂ (Fig. 4G and Table 7).

It is difficult to assign a specific explanation for the intra-sample grain age dispersion observed in some samples, but in all cases grain morphology shows either one or no crystal terminations. And, there is no significant correlation between age and eU content (Table 6). Besides those factors already discussed for zircon, (U-Th-Sm)/He age dispersion in apatite may be caused by the presence of U and/or Th-rich micro-inclusions, He implantation from external sources, grain breakage, or chemical effects (see Fitzgerald et al., 2006; Wildman et al., 2016).

4.3.4. Summary of thermochronologic data across all systems

A comparison of data from all three thermochronologic systems points to a High Himalaya region with rapid cooling and fast exhumation rates within the Plio-Quaternary time period, while the Lesser Himalaya region is characterized by relatively slower cooling

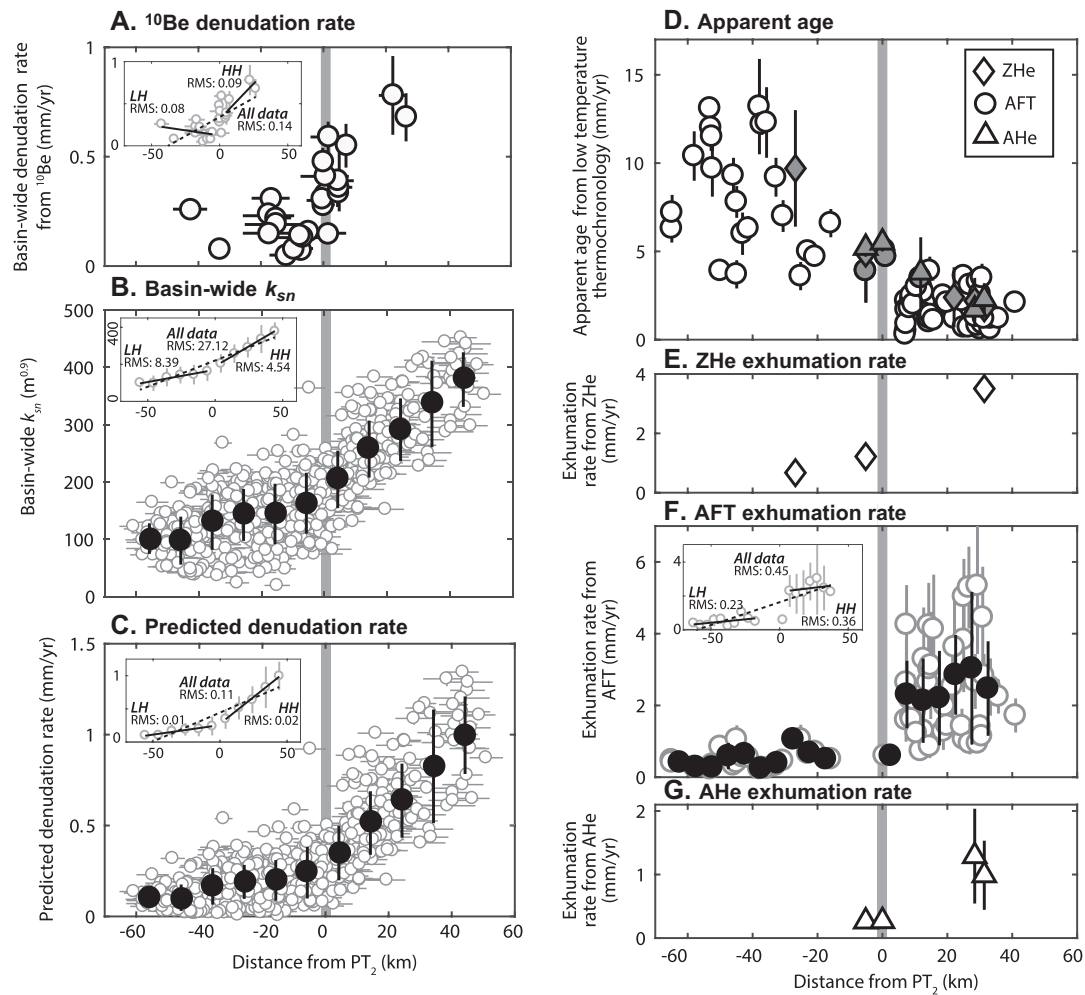


Fig. 4. A. Basin-wide denudation rate data calculated from ¹⁰Be concentrations versus distance from PT₂, where positive is hinterlandward (north) across strike. Uncertainties in distance reflect the size of the basin sampled. B. Basin-wide k_{sn} data plotted against distance from PT₂ and binned over 10-km-wide bins, showing mean and 1σ standard deviation in each bin. C. Predicted basin-wide erosion rate versus distance from PT₂. As in part B, data are binned over a distance of 10 km. D. Apparent ages from this (grey) and previous studies (white) for zircon Helium (ZHe),apatite fission track (AFT) and apatite Helium (AHe) versus distance from PT₂. See text and Fig. 3B for references to published cooling ages (Tables 4–6, A.1). E. ZHe exhumation rate versus distance from PT₂ (Table 7). F. AFT exhumation rate versus distance from PT₂. Individual samples shown in grey, with mean and standard deviation of data over 5 km bins shown in black (Tables 7 and A.1). G. AHe exhumation rate versus distance from PT₂ (Table 7). Insets show linear fits to the data for either the whole dataset (all data, dashed line), or separate fits for the Lesser Himalaya (LH) and High Himalaya (HH) regions individually (solid lines). All fits are linear least-squares fits, with root mean square error (RMS) shown. For data in insets A and F, data that lie across the PT₂ were excluded from the LH and HH fits, but were included in the all data fit.

and lower exhumation rates since as early as the late Miocene (Figs. 3 and 4). In the High Himalaya region north of the PT₂, late Neogene rapid cooling explains the rough equivalency, and in some instances overlap within age uncertainties, between the ZHe, AFT and AHe apparent ages (samples IN-12-08 and IN-12-09, Tables 5–7 and Fig. 4). In the Lesser Himalaya region south of the PT₂, the apparent ages from all three thermochronologic systems are also roughly equivalent to one another for a given position along strike with some exceptions. Fig. 4 shows that some of the calculated ZHe exhumation rates are faster than calculated AHe and AFT exhumation rates for a similar position relative to the PT₂. Although these observations might imply faster erosion rates in the late Miocene to Pliocene, more samples and/or alternate methods are required to confidently test this hypothesis. In one instance, the AHe age (5.1 ± 2.7 Ma, sample 14, Table 6) is slightly older than the ZHe age from the same sample (4.9 ± 0.6 Ma, sample 5, Table 4). Although the uncertainties between the weighted mean ages overlap, we suggest that this apparent discrepancy may be due to factors related to the dispersion of AHe ages in this sample.

Although the thermochronologic samples collected span $> \sim 3$ km in elevation, we observe no strong correlation of apparent age or exhumation rate with elevation. In fact, samples collected at lower

elevations on average exhibit older apparent ages, in a trend opposite to what would be expected under conditions of uniform cooling or uniform exhumation (Fig. 3B). Thus, despite the differences in detail, the first order signal from the thermochronologic data point to a distinct decrease in apparent ages northwards across the PT₂, and a corresponding increase in exhumation rate since at least the Plio-Quaternary for the High Himalaya region but spanning into the late Miocene for the Lesser Himalaya region.

4.4. Comparison of thermochronologic and ¹⁰Be-derived absolute erosion rates

Both ¹⁰Be-derived and thermochronologic data exhibit marked gradients across the PT₂, but the long-term erosion rates we estimate using thermochronology are higher than the short-term denudation rates estimated by ¹⁰Be cosmogenic analyses by as much as an order of magnitude (Figs. 3 and 4). Taken at face value, this difference between long and short-term absolute erosion rates could reflect an overall slowing down of erosion rates from the late Miocene-Pleistocene into the Holocene due to an equivalent decrease in rock uplift rates. While this hypothesis is tentatively supported by the observation of slightly

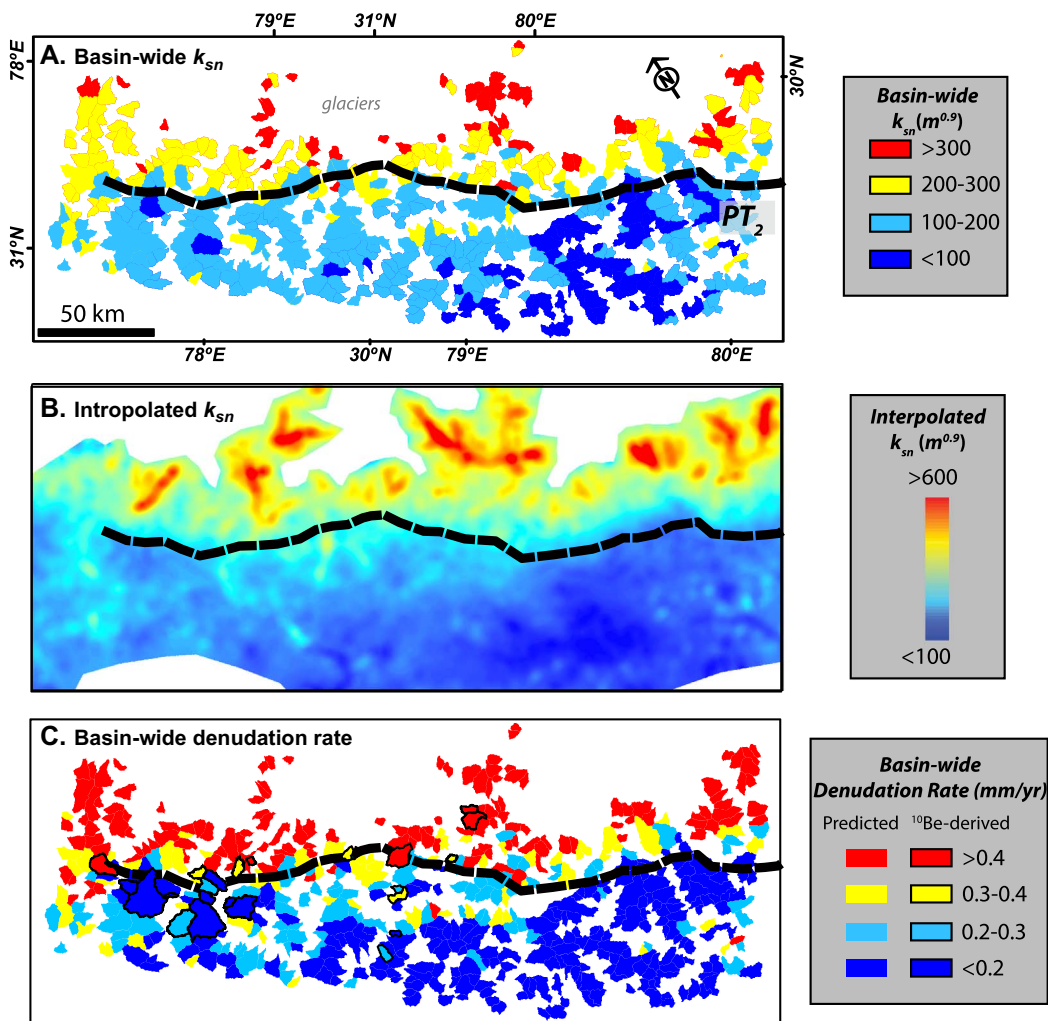


Fig. 5. A. Basin-averaged normalized river channel steepness (k_{sn}) calculated using the integral method. B. Interpolated k_{sn} calculated from k_{sn} data from Morell et al. (2015). C. Predicted and ^{10}Be -derived basin-wide denudation rate. PT₂ shown by dashed black line in all figures. The same map extent and scale are shown in all figures.

faster ZHe exhumation rates than AFT exhumation rates in the Lesser Himalaya south of the PT₂ (Fig. 4), given recent discussions about these topics in the literature (Finnegan et al., 2014; Ganti et al., 2016), we suggest several caveats should be taken into account before coming to this conclusion.

First, our modeling of the thermochronologic data was not designed to evaluate absolute erosion rates, and was instead designed to estimate relative rates of exhumation and trends across the PT₂. Exhumation rates modeled using the 1D approach used here are highly dependent upon the choice of geothermal gradient. Although we have no direct data upon which to change our initial assumption of a 35–45 °C/km geothermal gradient (Willett and Brandon, 2013), using a higher geotherm may be more applicable and would result in lower absolute exhumation rates. Second, paleo-erosion rate analyses show that erosion rates could have been as much as 2–4 times higher during the last glaciation in this region of the Himalaya ~16 ka (Scherler et al., 2015). Thus, the higher long-term exhumation rates calculated from thermochronology (Tables 7 and A.1) could simply reflect the time-averaged rate of erosion across multiple glacial-interglacial cycles that is not captured by the ^{10}Be denudation rate data. Given the time period implied by even the slowest denudation rates (0.05 mm/yr over ~10,000 years) (Tables 1 and 2), the analyzed ^{10}Be samples should not have been influenced by increases in erosion rate related to the last glaciation at ~16 ka (Scherler et al., 2015). Finally, despite the care that we took to sample basins without obvious terraces or landslides,

the ^{10}Be abundance in ^{10}Be samples could be influenced by poor mixing of the sampled sediment, which could lead to variations in the absolute values determined by our ^{10}Be -derived denudation rate analysis. While all of these factors could lead to differences in absolute erosion rates between the long- and short-term erosion rates analyzed, they would not influence the relative rates of erosion across the PT₂ that we are interested in evaluating here.

5. Discussion

5.1. Implications for active fault kinematics

To a first order, the results show a distinct northward increase in millennial denudation rates across the PT₂ that spatially coincides with an abrupt increase in exhumation rates averaged over million year time scales (Figs. 3 and 4). This close spatial similarity in relative rates of long- (Ma) and short-term (ka) erosion suggests that this gradient in erosion rates has persisted in the same relative position since at least the past ~1.5 Ma, the minimum time period encompassed by the majority of the thermochronologic samples. Assuming that the gradients in long and short time scale erosion rates across the PT₂ (Fig. 4) reflect rates of rock uplift, as is suggested by the landscape metrics (Figs. 4 and 5), this pattern of rock uplift rates would have similarly persisted across the PT₂ since at least ~1.5 Ma to present. The persistence of a distinct change in vertical rock uplift rates across the PT₂ over a million year

Table 3Properties of basins sampled for ^{10}Be denudation rates.

Sample #	Drainage area [km ²]	Basin relief ^a [m]	Basin-wide hillslope ^b angle [deg]	Basin-wide mean annual rainfall ^c [mm/yr $\pm 1\sigma$]	Basin-wide k_{sn} , slope-area method ^d [m ^{0.9} $\pm 1\sigma$]	Basin-wide k_{sn} integral method ^e [m ^{0.9}]	R ² on elevation- χ fit
1	27.5	1689	27	1278 \pm 65	124 \pm 21	140 \pm 1	0.99
2	71.5	2622	27	2453 \pm 428	201 \pm 41	217 \pm 1	0.97
3	18.2	2052	29	2575 \pm 303	195 \pm 19	238 \pm 1	0.99
4	7.8	1680	26	3008 \pm 63	–	235 \pm 1	1.00
5	3.8	1547	27	2987 \pm 33	–	231 \pm 4	0.98
6	25.9	1536	27	1069 \pm 23	–	141 \pm 1	0.98
7	9.5	1394	32	1537 \pm 129	–	173 \pm 1	1.00
8	11.0	1645	27	1177 \pm 22	120 \pm 16	184 \pm 1	0.99
9	88.6	1985	27	1524 \pm 178	163 \pm 33	155 \pm 1	0.97
11	24.7	2292	31	2759 \pm 124	193 \pm 41	216 \pm 1	0.98
12	9.0	1249	25	1637 \pm 213	–	144 \pm 1	0.99
13	88.6	1985	27	1524 \pm 178	163 \pm 33	155 \pm 1	0.97
14	210.0	2027	24	1758 \pm 313	107 \pm 38	93 \pm 1	0.69
15	36.0	1201	28	2012 \pm 217	95 \pm 22	105 \pm 1	0.96
16	66.1	2448	33	2124 \pm 182	173 \pm 52	175 \pm 1	0.96
17	46.7	2817	31	2086 \pm 277	243 \pm 55	282 \pm 3	0.93
18	20.1	2475	28	2232 \pm 363	226 \pm 42	325 \pm 4	0.94
19	10.7	1946	30	1989 \pm 98	150 \pm 17	219 \pm 2	0.98
20	178.9	2103	25	1436 \pm 254	118 \pm 26	113 \pm 1	0.92
21	90.4	1919	28	1910 \pm 195	150 \pm 36	144 \pm 1	0.98
22	14.1	1698	30	1882 \pm 349	150 \pm 41	175 \pm 1	1.00
23	26.3	1671	27	1735 \pm 103	137 \pm 24	163 \pm 1	0.97
24	37.6	1997	29	1955 \pm 376	147 \pm 20	175 \pm 1	0.99
25	42.4	2288	28	2211 \pm 340	165 \pm 35	166 \pm 1	0.97
26	9.5	1861	28	2698 \pm 255	–	219 \pm 2	0.99
27	28.9	2576	33	2243 \pm 110	188 \pm 36	218 \pm 1	0.99

^a Calculated by subtraction of highest and lowest elevation in basin.^b Uncertainty fixed at 20 m due to standard precision of dataset (Falorni et al., 2005).^c Determined by resampling ~4-km TRMM data (Bookhagen and Burbank, 2006) to a 100-m resolution, and extrapolating the mean and standard deviation of raster values within each watershed area.^d Based on data in Morell et al. (2015). Dashed cells indicate basins smaller than the smoothing window used in calculations (10 km).^e Uncertainties on k_{sn} based on standard error of elevation- χ regression.

time scale has important implications for how strain is actively accumulating in the hinterland of this Himalayan region.

The inference that the PT₂ has maintained its relative position with respect to the overriding plate throughout the Quaternary argues against the overthrusting model shown in Figs. 1D and 7A. Overthrusting above a décollement ramp, in the absence of underplating or additional structures in the upper plate, would result in the progressive translation of upper plate rocks from areas of high rock uplift rate above the décollement ramp to areas of low rock uplift rate above the décollement flat (Fig. 7A). Under the assumption that exhumation rates from thermochronology reflect the accumulation of past and present rates of rock uplift, this scenario would lead to a steady and gradual decrease in rates of long term exhumation rates southward from the current position of the PT₂. But, instead both millennial and long-term erosion rates increase markedly at the current position of the PT₂ and are relatively invariant within the Lesser Himalayan region above the décollement flat (Fig. 4). Therefore, if there is a décollement ramp beneath the High Himalaya, as suggested by regional geophysical data (Caldwell et al., 2013), it may enhance rock uplift rates in the High Himalaya (Scherler et al., 2014). But, the physiographic and erosional data (Figs. 3–5) argue against passive overthrusting above the décollement ramp without additional active upper plate structures (Fig. 7A).

The simplest scenario for the observed erosional and landscape changes in this region (Figs. 3–5) contains an emergent fault located at the PT₂ (Wobus et al., 2006a) that roots into the décollement ramp (Figs. 1E and 7B). An emergent fault provides a simple explanation for the persistence of the PT₂ at the same relative location with respect to the upper plate throughout at least the past 1.5 Ma. While attractive for its simplicity, a surface-breaking fault at the PT₂ has yet to be identified in the field in this region and the PT₂ shows no direct relationship with lithologic contacts at the surface (Fig. 1C). Although this lack of direct field evidence could be due to the relatively poor exposure in this

highly vegetated region (Wobus et al., 2006a), if an emergent fault follows the entire length of the PT₂, it would be as much as 400 km long in this region. If slip along this large structure occurred for any extended period of time, it seems likely that such a large fault would eventually separate disparate lithologies that would be observable in the field.

The third kinematic model proposed for the region of Central Nepal contains an active blind duplex on the décollement ramp, which has been postulated to grow by accretion of underthrust material from the Indian plate and resultant slip along the basal fault(s) within the duplex (Fig. 1F) (Bollinger et al., 2004; Robert et al., 2009; Herman et al., 2010). In this model, only the basal-most horses are active at any given time and a roof thrust remains preserved. In our study area of Northwest India, such a duplex would explain the lack of clear field evidence for an abrupt change in lithology at the current position of the PT₂, as the active fault systems may remain buried beneath the surface (Fig. 7C). One implication of this model is that in order for the PT₂ to retain its relative position for the past 1.5 Ma, as our data suggest (Fig. 4), the relative magnitudes of underplating and overthrusting must match throughout this time period. As shown in Fig. 7C, if the location of the erosional front demarcated by the PT₂ continues to reflect an equilibrium with rock uplift rates produced by the underlying fault geometry, the PT₂ should shift forelandward or hinterlandward depending on whether the duplex is in a period of overthrusting or underplating. To a first order this duplex model predicts higher rock uplift rates for regions north of the PT₂ compared to regions south of the PT₂, but the spatial distribution of local time-averaged rock uplift rates could vary depending on the magnitude of overthrusting and/or underplating and the length of time between accretion and overthrusting events (Fig. 7C).

We propose a fourth option that is a hybrid of the emergent fault and duplex models wherein underplating occurs beneath the High

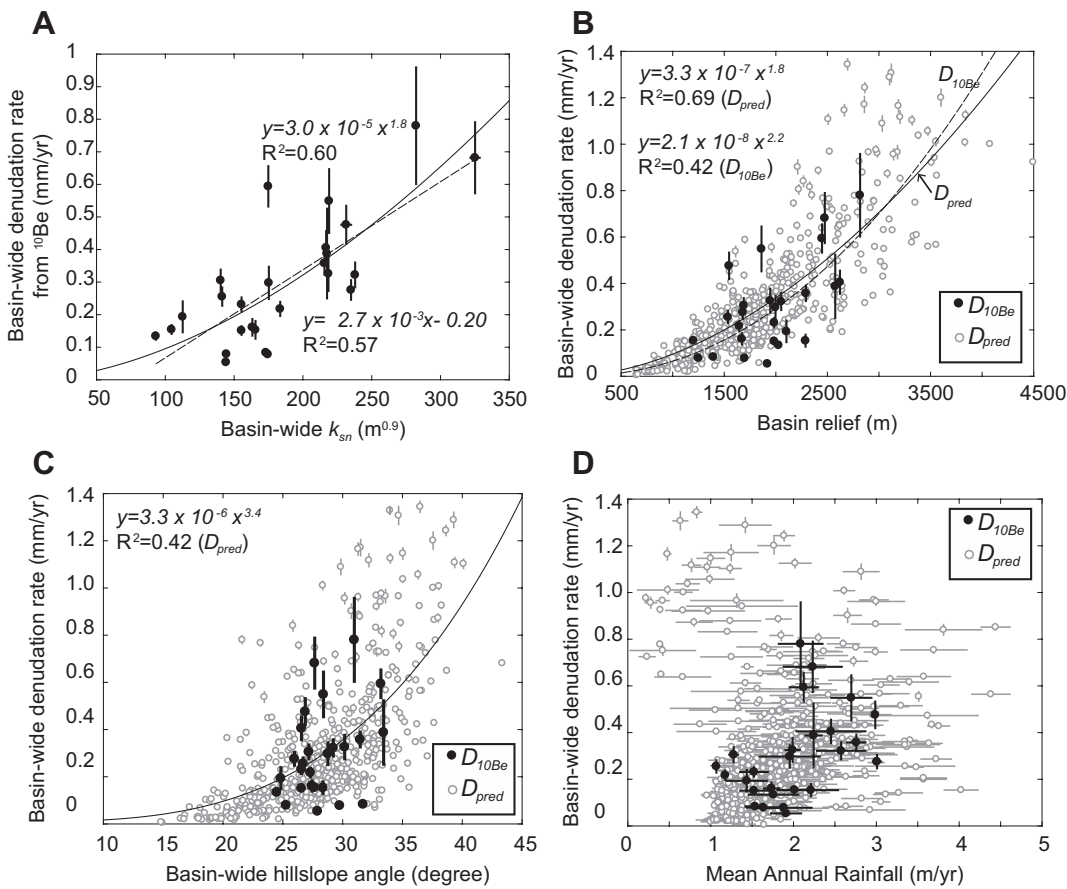


Fig. 6. A. Basin-wide denudation rate from ^{10}Be concentrations versus basin-wide k_{sn} calculated using the integral method. Power law (solid line) and linear (dashed line) fits to data are shown with their R^2 values. B. Basin-wide denudation rate versus basin relief for ^{10}Be -derived data ($D_{10\text{Be}}$) and predicted denudation rate (D_{pred}). Power law fits to the data are shown with a dashed line for $D_{10\text{Be}}$ and a solid line for D_{pred} . C. Basin-wide denudation rate versus basin-wide hillslope angle for $D_{10\text{Be}}$ (black) and D_{pred} (grey). Power law fit is based on D_{pred} . D. Basin-wide denudation rate versus mean annual rainfall from the TRMM dataset (Bookhagen and Burbank, 2006), showing no clear relationship. To determine average yearly rainfall within individual catchments, we resampled the ~4-km-resolution TRMM data to a 100-m resolution, and extrapolated the mean and standard deviation of raster values within each watershed area.

Himalaya but is accompanied by slip on one or more thrust horses within a duplex and/or imbricate fan either at the PT₂ or at higher elevations within the wedge (Fig. 7D). In a scenario similar to one proposed by Whipple et al. (2016) and Wobus et al. (2006a) for Central Nepal, we suggest that thrust faults within the imbricate stack of the High Himalaya may either break the surface at some locations along-strike or remain buried beneath the surface in other locations, and these faults may or may not extend for large distances (greater than tens of kilometers) along strike. Similar to the duplex model (Fig. 7C), this hybrid model would explain why there are not distinct contrasts in lithology across the entire length of the 400-km-long PT₂ in this region, while also allowing for active thrusting higher within the wedge above the décollement ramp.

Several observations suggest that active faulting occurs above the décollement ramp within the High Himalaya north of the PT₂. First, results by Kayal et al. (2003) suggest that aftershocks associated with the $M_w 6.3$ 28 March 1999 Chamoli earthquake (Fig. 8A) likely occurred on shallow thrust faults above the main décollement in our study area, in a manner similar to what has been hypothesized based on the locations of aftershocks of the Nepal earthquake (Whipple et al., 2016). Two, several authors suggest that the variability of AFT ages within the High Himalaya in the eastern portion of our study area is caused by recent slip along the emergent Munsigli and Vaikrita Thrusts, which are considered part of the Main Central Thrust zone (MT, VT on Fig. 1C) (e.g. Valdiya, 1980; Patel et al., 2007; Patel and Carter, 2009; Singh et al., 2012). Three, there is a steady increase in predicted denudation rates (and by definition k_{sn}) from the PT₂ northwards toward the

highest peaks of the Himalaya (Fig. 4A–C). If k_{sn} and predicted denudation rates in this region are proportional to millennial rock uplift rates as we suspect, then such a northward increase in rock uplift rate could be due to slip along emergent thrust faults within the High Himalaya imbricate stack and/or recent displacement along the South Tibetan fault system (Figs. 1C and 7D). Finally, the observation of intense microseismic activity within the upper 20 km of the crust in the High Himalaya region north of the PT₂ (Mahesh et al., 2013, 2015) (Fig. 8A), further suggests that active deformation frequently occurs above the décollement ramp within the orogenic wedge. The southernmost extent of this microseismic zone coincides remarkably well with the location of the PT₂ at the surface and further implies a connection between active hinterland strain accumulation and the development of the physiographic changes across the PT₂ (Fig. 8A). In summary, the erosional and landscape data (Figs. 3–5), when combined with regional patterns of seismicity, are best explained by a model that incorporates both underplating on the décollement ramp and emergent thrust faulting (Fig. 7D).

5.2. Relationship between denudation rate and precipitation rate

The landscape and erosional changes at the PT₂ also coincide with a band of heightened mean annual precipitation within the High Himalaya (Fig. 2C) (Bookhagen and Burbank, 2006), pointing to a strong coupling between surface erosion, active deformation, and climate. While these spatial coincidences imply that precipitation must be strongly coupled to tectonic processes, our observation of no direct

Table 4
Single grain zircon (U-Th)/He data^a.

Sample #	Lat. [deg N] ^b	Long. [deg E] ^b	Lab no.	He#	⁴ He [ncc]	Mass [mg]	Mean FT ^c	U [ppm]	Th [ppm]	Th/U [ppm]	Grain length [mm]	Grain half-width [mm]	Crystal morphology ^e	Corrected age [Ma ± 1σ]	Weighted mean age ^f [Ma]
<i>Bedrock samples north of PT₂</i>															
2 (IN1209)	30.55672	79.54517	9171	27714	0.249	0.0052	0.77	196.3	67.3	0.34	212.1	208.8	44.1	2T	1.8 ± 0.1
2 (IN1209)	30.55672	79.54517	9173	27718	0.666	0.0092	0.80	361.9	72.4	0.20	378.9	265.0	51.0	2T	1.6 ± 0.1
2 (IN1209)	30.55672	79.54517	9172	27919	1.596	0.0112	0.81	293.4	148.4	0.51	328.3	275.8	55.6	2T	3.6 ± 0.2
2 (IN1209)	30.55672	79.54517	9200	27844	0.198	0.0058	0.76	143.4	39.4	0.27	152.6	248.3	40.8	2T	1.8 ± 0.1
2 (IN1209)	30.55672	79.54517	9452	28469	0.504	0.0080	0.78	269.6	34.9	0.13	277.8	304.1	42.2	2T	1.9 ± 0.1
2 (IN1209)	30.55672	79.54517	9453	28471	0.536	0.0032	0.73	69.7	27.2	0.04	703.5	198.6	34.2	2T	1.9 ± 0.1
2 (IN1209)	30.55672	79.54517	9608	28919	0.427	0.0060	0.77	318.2	97.2	0.31	341.1	225.9	44.6	2T	1.7 ± 0.1
6 (IN1246)	30.88784	78.67252	9194	27828	0.576	0.0061	0.79	400.9	46.4	0.12	411.8	190.6	54.4	2T	1.8 ± 0.1
6 (IN1246)	30.88784	78.67252	9195	27822	1.373	0.0126	0.83	263.9	36.0	0.14	272.3	221.7	61.9	2T	3.3 ± 0.2
6 (IN1246)	30.88784	78.67252	9196	27820	0.870	0.0083	0.81	375.7	49.8	0.13	387.4	224.8	55.8	2T	2.2 ± 0.1
1 (IN1208)	30.53741	79.52383	9167	27670	2.433	0.0080	0.80	483.0	156.7	0.32	519.9	244.3	50.2	2T	4.8 ± 0.3
1 (IN1208)	30.53741	79.52383	9169	27700	1.667	0.0093	0.82	360.1	149.8	0.42	395.3	202.7	70.6	2T	3.7 ± 0.2
1 (IN1208)	30.53741	79.52383	9170	27716	0.743	0.0056	0.77	380.2	262.9	0.69	442.0	219.6	44.1	1T	2.5 ± 0.2
1 (IN1208)	30.53741	79.52383	9456	28716	4.346	0.0215	0.85	928.8	15.9	0.02	932.5	366.9	65.1	2T	1.8 ± 0.1
<i>Bedrock samples at or south of PT₂</i>															
5 (IN1233)	30.73825	78.35305	9190	27796	0.745	0.0049	0.76	225.9	91.2	0.40	247.3	204.6	43.1	2T	5.1 ± 0.3
5 (IN1233)	30.73825	78.35305	9191	27807	1.982	0.0061	0.79	526.3	99.5	0.19	549.7	204.5	49.5	2T	4.8 ± 0.3
5 (IN1233)	30.73825	78.35305	9192	27816	0.422	0.0036	0.74	143.9	102.1	0.71	167.7	167.9	42.5	2T	5.8 ± 0.4
5 (IN1233)	30.73825	78.35305	9457	28719	1.446	0.0040	0.74	582.3	241.9	0.42	639.1	207.9	37.4	2T	4.6 ± 0.3
5 (IN1233)	30.73825	78.35305	9458	28721	0.769	0.0041	0.74	319.3	131.9	0.41	350.3	200.5	39.2	2T	4.4 ± 0.3
3 (IN1221)	30.53752	78.33911	9187	27785	9.260	0.0047	0.77	1557.3	345.6	0.22	1638.6	181.9	47.5	2T	9.8 ± 0.6
3 (IN1221)	30.53752	78.33911	9188	27787	2.688	0.0046	0.76	525.2	111.7	0.21	551.5	192.8	43.8	2T	8.7 ± 0.5
3 (IN1221)	30.53752	78.33911	9189	27800	6.615	0.0091	0.78	499.7	84.5	0.17	519.5	349.2	41.0	2T	11.5 ± 0.7
4 (IN1226)	30.64371	78.32792	9197	27830	3.384	0.0141	0.84	284.4	57.6	0.20	298.0	255.2	70.5	2T	6.6 ± 0.4
4 (IN1226)	30.64371	78.32792	9199	27834	0.910	0.0032	0.72	295.3	159.2	0.54	332.7	186.6	35.7	2T	7.0 ± 0.4
4 (IN1226)	30.64371	78.32792	9207	27840	0.431	0.0059	0.79	425.9	55.7	0.13	439.0	183.2	66.1	2T	1.4 ± 0.1
4 (IN1226)	30.64371	78.32792	9206	27955	1.798	0.0012	0.64	841.4	960.0	1.14	1067.0	113.4	31.5	2T	11.1 ± 0.7
9 (IN1230)	30.68760	78.35824	9468	28935	1.483	0.0105	0.81	244.3	103.9	0.43	268.7	270.9	54.2	2T	4.3 ± 0.3
9 (IN1230)	30.68760	78.35824	9469	28937	4.229	0.0141	0.82	368.9	161.1	0.44	406.7	344.5	53.4	2T	6.0 ± 0.4
9 (IN1230)	30.68760	78.35824	9470	28939	0.909	0.0046	0.77	259.4	137.2	0.53	291.6	167.2	51.7	2T	5.6 ± 0.3
7 (IN1224)	30.61371	78.31520	9605	28957	0.530	0.0028	0.72	64.5	52.8	0.82	76.9	154.4	34.5	2T	20.1 ± 1.2
7 (IN1224)	30.61371	78.31520	9606	28949	7.158	0.0064	0.77	643.2	245.3	0.38	700.8	252.3	42.5	2T	13.1 ± 0.8
7 (IN1224)	30.61371	78.31520	9607	28942	4.649	0.0053	0.77	498.4	313.0	0.63	571.9	200.9	46.2	2T	12.6 ± 0.8
8 (IN1228)	30.67378	78.35484	9473	28749	5.132	0.0084	0.81	518.6	80.1	0.15	537.4	218.6	58.0	2T	9.3 ± 0.6
8 (IN1228)	30.67378	78.35484	9474	28747	4.277	0.0051	0.76	434.1	70.3	1.62	599.5	194.2	46.5	2T	15.3 ± 0.9
8 (IN1228)	30.67378	78.35484	9471	28945	2.098	0.0092	0.80	249.4	364.4	1.46	335.1	229.9	58.3	2T	11.4 ± 0.7
8 (IN1228)	30.67378	78.35484	9471	28945	2.098	0.0046	0.77	367.3	69.0	0.19	383.5	184.5	45.8	2T	9.8 ± 0.6

^a Analyses in italics excluded from calculation of weighted mean.

^b Latitude and longitude of bedrock sample. For detrital samples, the sample collection location at the outlet of the basin is indicated.

^c FT is the a-ejection correction after [Farley et al. \(1996\)](#).

^d Effective uranium concentration (U ppm ± 0.25 Th ppm).

^e Grain morphology: 0T = no terminations, 1T = one termination, 2T = two terminations.

^f Weighted mean age (uncertainties at the 95% confidence level) calculated by weighting assigned internal errors only using Isoplot v.4.15 ([Ludwig, 2012](#))

Table 5
New apatite fission track data.

Sample #	Lat. [deg N]	Long. [deg E]	No. of grains ^a	N _s ^b	p _s ^c [10 ⁵ cm ⁻²] ^d	²³⁸ U ^d [ppm ± 1σ] ^e	P(χ ²) ^f [%]	Dispersion [%]	Pooled age ^g [Ma ± 1σ]	Mean track length [μm ± se]	No. of lengths measured	St. dev. ^g [μm]	D _{par} ^h [μm]
North of PT ₂													
19 (IN1243)	30.80713	78.61980	9	15	0.375	31.08 ± 18.49	50.18	7.2	2.4 ± 1.0	—	—	—	
At or south of PT ₂													
17 (IN1215)	30.37208	79.31190	33	204	1.143	54.96 ± 30.99	58.65	33.0	4.4 ± 0.5	13.55 ± 0.16	63	1.27	
18 (IN1233)	30.73825	78.35505	3	5	0.674	30.05 ± 27.98	25.83	30.0	4.2 ± 2.4	—	—	1.02 ± 0.04	

^a No. of grains used for apatite age determination.

^b N_s = number of spontaneous tracks counted.

^c p_s = spontaneous track density.

^d ²³⁸U = average uranium content of all grains measured by LA-ICP-MS.

^e P(χ²) = probability of χ² for (n – 1) degrees of freedom (Galbraith, 1981).

^f T_{pool} = AFT pooled U age calculated from pooled N_s and ²³⁸U concentration measured by LA-ICP-MS.

^g Standard deviation of track length distribution.

^h D_{par} = long axis of track etch pit parallel to the c-axis.

relationship in plots of denudation rate versus yearly precipitation (Fig. 6D) indicates that if there is a relationship between rates of precipitation and erosion, it is likely a secondary effect. As suggested by Bookhagen and Burbank (2006), the change in relief due to enhanced rock uplift rates north of the PT₂ likely enhances orographic precipitation. But our data (Fig. 6D) and those of others from similar study areas throughout the Himalayan arc (e.g. Godard et al., 2014) suggest that while precipitation likely plays a role, the enhanced rock uplift rates inferred at this hinterland location are unlikely to be driven by precipitation alone.

5.3. What controls the localization and persistence of the PT₂?

The results show a compelling relationship between gradients in long- and short-term erosion rates (Figs. 4 and 5), heightened deformation and increased shallow seismicity across the PT₂ (Fig. 8A) (Mahesh et al., 2013, 2015). Interestingly, all of these processes occurring across the PT₂ appear to lie along a small circle that, with a few exceptions (e.g. Harvey et al., 2015), spans for most of the length of the Himalaya arc and is positioned approximately 100 km across strike from the Main Frontal Thrust (Fig. 1B) (Bilham et al., 1997; Bendick and Bilham, 2001). The continuation of this small circle over such a long distance (1000s of km) implies that the processes occurring across the PT₂ could be due to temperature and/or rheology. Recent analyses of GNSS data show that the erosional and deformational front marked by the PT₂ in our study area also coincides with the northernmost, down-dip extent of the geodetically locked portion of the décollement (Stevens and Avouac, 2015) (Fig. 8B). The position of the downdip extent of the equivalent locked zone in Central Nepal has been shown to roughly coincide with the depth at which temperatures approach or exceed 300–350 °C on the décollement thrust (Avouac, 2003; Herman et al., 2010; Stevens and Avouac, 2015). The décollement within the study area may approach similar ~350° temperatures at depth beneath the current location of the PT₂, given the highly similar décollement geometries between the two regions. Laboratory experiments show that quartz-rich rocks transition from velocity-weakening to velocity-strengthening near the ~350 °C isotherm, as quartz transitions from brittle to semi-brittle behavior (Blanpied et al., 1995). Dehydration reactions have also been shown to occur at this temperature, which can result in a decrease in effective stress, as pore fluid pressure is increased (Blanpied et al., 1995). Both of these processes could promote slip along either the basal décollement or overlying crustal faults within the High Himalaya (Hyndman and Wang, 1993). If any or all of these temperature-controlled processes are taking place, it could explain why there has been a persistent localization of the tectonic and erosional processes at the PT₂ over the past 1.5 Ma or more (Figs. 3–5).

5.4. Implications for seismic cycle processes

The fact that the highest topography and inferred millennial rock uplift rates occur within the creeping section north of the PT₂ (Figs. 4 and 8) implies that at least some fraction of permanent strain accumulation occurs during the interseismic period between large earthquakes (Stevens and Avouac, 2015). Observations during the 2015 Nepal earthquake agree with this hypothesis. The 2015 Nepal earthquake nucleated at the down-dip edge of the locked zone in Central Nepal (Avouac et al., 2015), a zone that is similarly positioned to the south of the PT₂ as in our study area of Northwest India (Fig. 8B). InSAR and GNSS data indicate that the area north of the PT₂ of Central Nepal underwent co-seismic subsidence during the 2015 earthquake, while the areas south of the PT₂ experienced co-seismic uplift (Galetzka et al., 2015; Lindsey et al., 2015; Wang and Fialko, 2015; Whipple et al., 2016). These co-seismic observations stand in contrast to geomorphic, erosional and GNSS data from Central Nepal that show that the areas north of the PT₂ exhibit higher rates of net rock uplift over 10⁴–10⁶ year time scales by comparison to areas to the south (Lavé and Avouac,

Table 6
Single grain apatite (U-Th-Sm)/He data^a.

Sample #	Lat. [deg N]	Lon. [deg E]	Lab. No.	He#	⁴ He [ncc]	Mass [mg]	Mean F _T ^b	U [ppm]	Th [ppm]	Sm [ppm]	Th/U	[eu] [ppm] ^c	Grain length [mm]	Grain half-width [mm]	Crystal morphology ^d	Corrected age [Ma ± 1σ] [Ma] ^e
<i>North of PT₂</i>																
11(INI208)	30.53741	79.52383	8780	26440	0.037	0.0051	0.76	48.5	4.3	105.2	0.09	49.5	163.8	55.6	OT	1.6 ± 0.1
11(INI208)	30.53741	79.52383	8841	26569	0.051	0.0156	0.83	12.0	1.2	36.5	0.10	12.3	258.9	77.3	OT	2.6 ± 0.2
11(INI208)	30.53741	79.52383	8944	26905	0.139	0.0127	0.81	42.7	186.1	129.8	4.35	86.4	209.3	77.6	OT	1.3 ± 0.1
11(INI208)	30.53741	79.52383	8997	27103	0.039	0.0193	0.85	10.8	1.1	45.6	0.11	11.1	234.1	90.5	OT	1.8 ± 0.1
							1.7									1.7 ± 0.6
12(INI209)	30.55672	79.54517	8777	26434	0.069	0.0093	0.81	22.7	2.1	56.3	0.09	23.2	277.0	69.7	IT	3.2 ± 0.2
12(INI209)	30.55672	79.54517	8778	26436	0.160	0.0129	0.80	30.4	144.6	84.3	4.76	64.4	263.5	69.8	OT	2.0 ± 0.1
12(INI209)	30.55672	79.54517	8941	26913	0.051	0.0048	0.76	33.8	3.9	60.2	0.11	34.7	157.9	55.0	OT	3.3 ± 0.2
12(INI209)	30.55672	79.54517	9000	27115	0.052	0.0079	0.79	32.3	2.9	58.7	0.77	33.0	246.9	56.5	IT	2.1 ± 0.1
																2.3 ± 0.9
10(INI207)	79.507242	30.526251	8788	26449	0.329	0.0082	0.79	19.4	9.4	193.5	0.49	21.6	203.8	63.4	OT	19 ± 1.0
10(INI207)	79.507242	30.526251	8840	26567	0.327	0.0117	0.82	19.3	2.8	394.2	0.14	20.0	250.0	68.4	OT	14 ± 1.0
10(INI207)	79.507242	30.526251	8787	26451	0.422	0.0081	0.81	21.7	16.5	347.0	0.76	25.6	205.5	79.8	IT	21 ± 1.0
10(INI207)	79.507242	30.526251	8996	27105	0.057	0.0075	0.77	5.9	14.1	107.0	2.40	9.2	189.2	62.6	OT	8.7 ± 0.5
16(INI246)	30.88784	78.67252	8792	26473	0.685	0.0126	0.82	18.3	2.6	132.8	0.14	18.9	242.7	71.9	OT	29 ± 2
16(INI246)	30.88784	78.67252	8794	26484	0.417	0.0026	0.68	14.6	21.7	193.5	1.49	19.7	209.0	41.7	IT	97 ± 6.0
16(INI246)	30.88784	78.67252	9003	27125	0.602	0.0388	0.87	15.9	11.0	152.1	0.69	18.5	296.6	114.0	OT	34 ± 2.0
15(INI243)	30.80713	78.61984	8842	26575	0.194	0.0260	0.86	12.6	1.3	90.7	0.10	12.9	297.7	93.2	OT	5.5 ± 0.3
15(INI243)	30.80713	78.61984	8937	26929	0.064	0.0069	0.76	18.0	7.1	152.7	0.39	19.7	249.1	52.3	OT	5.1 ± 0.3
15(INI243)	30.80713	78.61984	8938	26923	0.129	0.0095	0.80	39.1	58.5	206.1	1.50	52.8	268.4	71.9	IT	2.6 ± 0.2
15(INI243)	30.80713	78.61984	9002	27119	0.196	0.0230	0.86	21.4	2.5	130.7	0.12	22.0	223.8	101.1	OT	3.7 ± 0.2
<i>At or south of PT₂</i>																
14(INI233)	30.73825	78.35305	8790	26469	0.051	0.0042	0.75	16.4	9.9	708.5	0.61	18.7	187.7	58.5	IT	6.7 ± 0.4
14(INI233)	30.73825	78.35305	8936	26931	0.052	0.0021	0.67	64.9	17.6	599.3	0.27	69.0	118.5	41.9	OT	4.3 ± 0.3
14(INI233)	30.73825	78.35305	10398	30875	0.547	0.0064	0.77	21.6	11.8	358.5	0.55	24.4	218.5	54.2	OT	5.1 ± 0.3
13(INI215)	30.37208	79.31190	8783	26465	0.759	0.0249	0.87	46.3	23.6	614.1	0.51	51.8	279.4	123.1	IT	5.4 ± 0.3
13(INI215)	30.37208	79.31190	8939	26921	0.257	0.0145	0.82	24.4	29.2	152.3	1.19	31.3	214.8	81.9	OT	5.6 ± 0.4
13(INI215)	30.37208	79.31190	9460	28656	1.581	0.0443	0.88	45.8	21.7	520.4	0.47	50.9	528.7	108.0	IT	6.5 ± 0.4
13(INI215)	30.37208	79.31190	8940	26919	0.290	0.0052	0.75	66.0	30.5	531.2	0.46	73.2	176.4	54.0	OT	8.3 ± 0.5
																5.7 ± 1.4

^a Samples in italics excluded from further analysis. Samples exhibited significant variability within single grain ages, and sample 16 was significantly older than surrounding regions by an order of magnitude (see text).

^b F_T is the α-ejection correction after Farley et al. (1996).

^c Effective uranium concentration (U ppm ± 0.235 Th ppm).

^d Grain morphology: OT = no terminations, IT = one termination, 2T = 2 terminations.

^e Weighted mean age (uncertainties at the 95% confidence level) calculated by weighting assigned internal errors only using Isoplot v.4.15 (Ludwig, 2012).

Table 7

Exhumation rates calculated from new thermochronology samples in this study.

Sample #	System ^a	Apparent age [Ma] ^b	Elevation [m]	Mean elevation [m ± 1σ] ^c	Difference from mean elevation [km]	Exhumation rate ^d [mm/yr]
North of PT_2						
12 (IN-12-9)	AHe	2.3 ± 0.9	1928	1967 ± 382	0.0	1.0 ± 0.5
11 (IN-12-8)	AHe	1.7 ± 0.6	1709	1938 ± 409	-0.2	1.3 ± 0.7
2 (IN-12-9)	ZHe	1.8 ± 0.1	1928	1967 ± 382	0.0	3.5 ± 0.2
At or south of PT_2						
13 (IN-12-15)	AHe	5.7 ± 1.4	1012	1221 ± 228	-0.2	0.3 ± 0.1
14 (IN-12-33)	AHe	5.1 ± 2.7	1011	1314 ± 211	-0.3	0.4 ± 0.3
17 (IN-12-15)	AFT	4.4 ± 0.5	1012	1221 ± 228	-0.2	0.7 ± 0.2
3 (IN-12-21)	ZHe	9.7 ± 3.3	924	1061 ± 227	-0.1	0.7 ± 0.3
5 (IN-12-33)	ZHe	4.9 ± 0.6	1011	1314 ± 211	-0.3	1.2 ± 0.4

^a AFT = apatite fission track; AHe = apatite (U-Th-Sm)/He; ZHe = zircon (U-Th)/He.^b See Tables 4–6 for apparent ages and source of uncertainties.^c Calculated over a ~2.5 km radius circle using SRTM 30-m data.^d Calculated using methods outlined in Willett and Brandon (2013).

2001; Wobus et al., 2006a; Robert et al., 2009; Herman et al., 2010; Godard et al., 2014), with a pattern highly similar to what we observe in our study area (Figs. 3–5). Given the numerous similarities in the distribution of aseismic creep, rock uplift rates and erosion rates between our study area and the region of Central Nepal affected by the 2015 earthquake, it is probable that similar seismic cycle processes are also operating in the study area in the Indian Himalaya. If so, and given

the lack of a large seismic event since 1803 ($M_w \sim 7.7$) in this region (Rajendran and Rajendran, 2005), Northwest India could be afflicted by earthquakes similar in size or larger than the 2015 Nepal event, especially if the event ruptures to the surface at the Main Frontal Thrust.

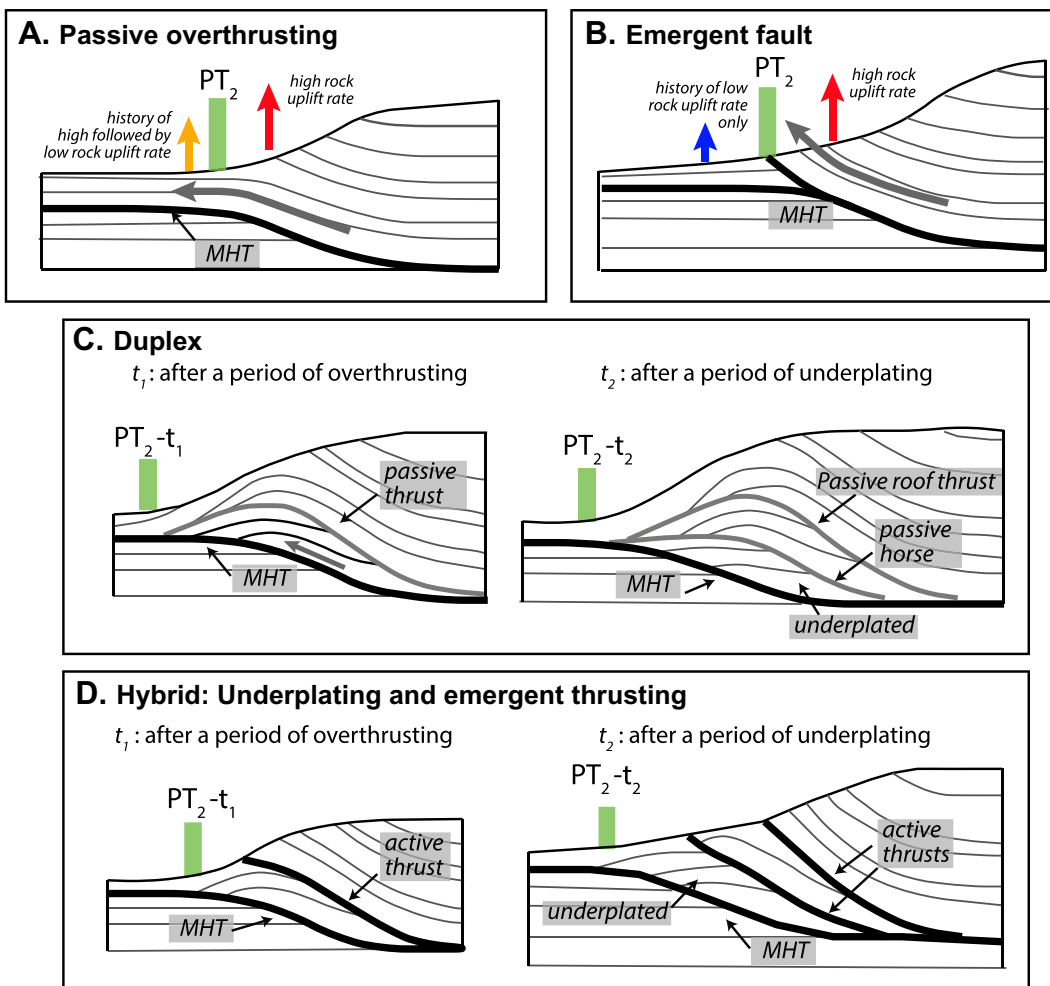


Fig. 7. Cartoons showing kinematic models discussed in text. A. Passive ramp overthrusting model (e.g. Cattin and Avouac, 2000) showing how rocks in the upper plate transition from a region of relatively high to relatively low rock uplift rate. B. Emergent fault model (e.g. Wobus et al., 2006a). C. Passive duplex model (e.g. Bollinger et al., 2004; Herman et al., 2010). D. Combined underthrusting and emergent faulting model (e.g. Whipple et al., 2016). Parts C and D show hypothetical scenarios for thrust geometries after a period of overthrusting (left, t_1) or underplating (right, t_2). In parts C and D, passive faults are shown in grey and active faults in black. MHT, Main Himalayan Thrust décollement.

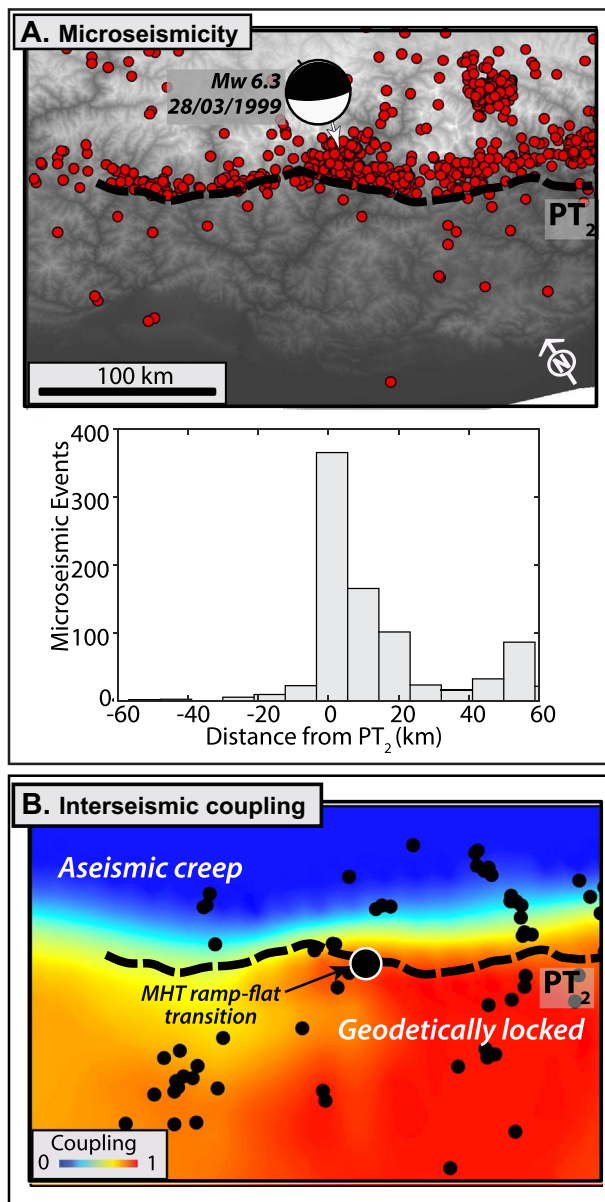


Fig. 8. A. Relocated microseismicity data ($M_w = 1-5$) from a local seismic network deployed from April 2005 to June 2008 (Mahesh et al., 2013). Focal mechanism of the M_w 6.3 28 March 1999 Chamoli earthquake shown (Kayal et al., 2003). Histogram shows number of microseismic events in each bin, relative to distance across strike from the PT₂. B. Map of interseismic coupling ratio from Stevens and Avouac (2015) calculated using compiled geodetic data (Banerjee and Bürgmann, 2002; Jade et al., 2014) and smoothed in this study using a kriging function. A coupling value of 1 indicates full locking, while a value of 0 means fully creeping. Small black dots indicate GNSS station locations. Black dot with white outline represents the map view location of the ramp-flat transition in the Main Himalayan Thrust (MHT) as revealed by receiver functions (Caldwell et al., 2013). Map extent for both panels is the same as Fig. 2, with location shown in Fig. 1B.

6. Conclusions

Distinctive northward increases in landscape morphology, channel steepness and millennial denudation rates across the PT₂ spatially coincide with an abrupt increase in exhumation rates averaged over at least the past 1.5 Ma in the Northwest Indian Himalaya. When viewed in the context of mapped geologic units and regional seismicity patterns, we suggest that the persistence of this erosion front over such a long (Ma) time scale is best explained by a kinematic model that incorporates both underplating on the décollement ramp and emergent thrust faulting. The close spatial relationship between the

physiographic and erosional changes across the PT₂ with both increased microseismicity at ≤ 20 km depth and the position of aseismic creep on the décollement thrust, implies a rheologic or temperature control on the position of the PT₂. This hypothesis is supported by the observation that the PT₂ appears to lie ~ 80 –100 km across strike from the Main Frontal Thrust for a significant length of the Himalayan arc. The co-location of regions of high millennial rock uplift rates with areas of aseismic décollement creep suggests that some portion of permanent strain accumulation occurs during the interseismic period between large earthquakes.

Supplementary data to this article can be found online at <http://dx.doi.org/10.1016/j.tecto.2017.09.007>.

Acknowledgements

Funding was provided by an NSERC Discovery grant, the Australian Research Council (DP140104056), and builds on a program supported by the Australia-India Strategic Research Fund. The University of Melbourne thermochronology laboratory receives infrastructure support under the AuScope Program of NCRIS. We are grateful to Abaz Alimanovic and Ling Chung for assistance with ZHe, AFT and AHe analyses. We thank V. Stevens for help with microseismicity data and D. Fink for cosmogenic analyses.

References

- Adams, B., Hodges, K., Whipple, K., Ehlers, T., van Soest, M., Wartho, J., 2015. Constraints on the tectonic and landscape evolution of the Bhutan Himalaya from thermochronometry. *Tectonics* 34 (6), 1329–1347.
- Ahmad, T., Harris, N., Bickle, M., Chapman, H., Bunbury, J., Prince, C., 1999. Isotopic constraints on the structural relationships between the Lesser Himalayan Series and the High Himalayan Crystalline Series, Garhwal Himalaya. *Geol. Soc. Am. Bull.* 112 (3), 467–477.
- Avouac, J.-P., 2003. Mountain building, erosion, and the seismic cycle in the Nepal Himalaya. *Adv. Geophys.* 46, 1–80.
- Avouac, J.-P., Meng, L., Wei, S., Wang, T., Ampuero, J.-P., 2015. Lower edge of locked main Himalayan thrust unzipped by the 2015 Gorkha earthquake. *Nat. Geosci.* 8 (9), 708–711.
- Balco, G., Stone, J.O., Lifton, N.A., Dunai, T.J., 2008. A complete and easily accessible means of calculating surface exposure ages or erosion rates from ^{10}Be and ^{26}Al measurements. *Quat. Geochronol.* 3 (3), 174–195 (Aug.).
- Banerjee, P., Bürgmann, R., 2002. Convergence across the northwest Himalaya from GPS measurements. *Geophys. Res. Lett.* 29 (13), 30–31.
- Bendick, R., Bilham, R., 2001. How perfect is the Himalayan arc? *Geology* 29 (9), 791–794.
- Bierman, P., Steig, E.J., 1996. Estimating rates of denudation using cosmogenic isotope abundances in sediment. *Earth Surf. Process. Landf.* 21 (2), 125–139.
- Bilham, R., Larson, K.P., Freymueller, J.T., et al., 1997. GPS measurements of present-day convergence across the Nepal Himalaya. *Nature* 386, 61–64.
- Blanpied, M.L., Lockner, D.A., Byerlee, J.D., 1995. Frictional slip of granite at hydrothermal conditions. *J. Geophys. Res. Solid Earth* 100 (B7), 13045–13064.
- Bollinger, L., Avouac, J.P., Beyssac, O., Catlos, E.J., Harrison, M.T., Grove, M., Goffé, B., Sapkota, S., 2004. Thermal structure and exhumation history of the Lesser Himalaya in central Nepal. *Tectonics* 23 (5).
- Bollinger, L., Sapkota, S.N., Tapponnier, P., Klinger, Y., Rizza, M., Van Der Woerd, J., Tiwari, D., Pandey, R., Birri, A., Bes de Berc, S., 2014. Estimating the return times of great Himalayan earthquakes in eastern Nepal: evidence from the Patu and Bardibas strands of the main frontal thrust. *J. Geophys. Res. Solid Earth* 119 (9), 7123–7163.
- Bookhagen, B., Burbank, D., 2006. Topography, relief and TRMM-derived rainfall variations along the Himalaya. *Geophys. Res. Lett.* 33 (L08405), 1–5.
- Burbank, D.W., Blythe, A.E., Putkonen, J., Pratt-Sitaula, B., Gabet, E., Oskin, M., Barros, A., Ojha, T.P., 2003. Decoupling of erosion and precipitation in the Himalayas. *Nature* 426 (6967), 652–655.
- Burchfiel, B.C., Zhiliang, C., Hodges, K.V., Yuping, L., Royden, L.H., Changrong, D., Jiene, X., 1992. The South Tibetan detachment system, Himalayan orogen: extension contemporaneous with and parallel to shortening in a collisional mountain belt. *Geol. Soc. Am. Spec. Pap.* 269, 1–41.
- Caldwell, W., Klemperer, S., Lawrence, J., Rai, S.S., Ashish, 2013. Characterizing the main Himalayan thrust in the Garhwal Himalaya, India with receiver function CCP stacking. *Earth Planet. Sci. Lett.* 367, 15–27.
- Cattin, R., Avouac, J.P., 2000. Modeling mountain building and the seismic cycle in the Himalaya of Nepal. *J. Geophys. Res.* 105 (B6), 13389–13407.
- Célérrier, J., Harrison, M.T., Webb, A.A.G., 2009a. The Kumaun and Garhwal Lesser Himalaya, India: part 1. Structure and stratigraphy. *Geol. Soc. Am. Bull.* 121 (9/10), 1262–1280.
- Célérrier, J., Harrison, T.M., Beyssac, O., Herman, F., Dunlap, W.J., Webb, A.A.G., 2009b. The Kumaun and Garhwal Lesser Himalaya, India: part 2. Thermal and deformation histories. *Geol. Soc. Am. Bull.* 121 (9/10), 1281–1297.

- Chmeleff, J., von Blanckenburg, F., Kossert, K., Jakob, D., 2010. Determination of the ^{10}Be half-life by multicollector ICP-MS and liquid scintillation counting. *Nucl. Inst. Methods Phys. Res. B* 268 (2), 192–199 Jan.
- Codilean, A.T., 2006. Calculation of the cosmogenic nuclide production topographic shielding scaling factor for large areas using DEMs. *Earth Surf. Process. Landf.* 31 (6), 785–794.
- Cyr, A.J., Granger, D.E., Olivetti, V., Molin, P., 2010. Quantifying rock uplift rates using channel steepness and cosmogenic nuclide-determined erosion rates: examples from northern and southern Italy. *Lithosphere* 2 (3), 188–198.
- Danišák, M., McInnes, B.I., Kirkland, C.L., McDonald, B.J., Evans, N.J., Becker, T., 2017. Seeing is believing: visualization of He distribution in zircon and implications for thermal history reconstruction on single crystals. *Sci. Adv.* 3 (2), e1601121.
- Denolle, M.A., Fan, W., Shearer, P.M., 2015. Dynamics of the 2015 M7.8 Nepal earthquake. *Geophys. Res. Lett.* 42 (18), 7467–7475.
- DiBiase, R.A., Whipple, K.X., 2011. The influence of erosion thresholds and runoff variability on the relationships among topography, climate, and erosion rate. *J. Geophys. Res. Earth Surf.* 116 (F4), 1–17.
- DiBiase, R.A., Whipple, K.X., Heimsath, A.M., Ouimet, W.B., 2010. Landscape form and millennial erosion rates in the San Gabriel Mountains, CA. *Earth Planet. Sci. Lett.* 289 (1–2), 134–144.
- Dodson, M.H., 1973. Closure temperature in cooling geochronological and petrological systems. *Contrib. Mineral. Petrol.* 40 (3), 259–274.
- Dunai, T.J., 2000. Scaling factors for production rates of in situ produced cosmogenic nuclides: a critical reevaluation. *Earth Planet. Sci. Lett.* 176 (1), 157–169.
- Elliott, J., Jolivet, R., González, P., Avouac, J.-P., Hollingsworth, J., Searle, M., Stevens, V., 2016. Himalayan megathrust geometry and relation to topography revealed by the Gorkha earthquake. *Nat. Geosci.* 9 (2), 174–180.
- Falorni, G., Teles, V., Vivoni, E.R., Bras, R.L., Amaralunga, K.S., 2005. Analysis and characterization of the vertical accuracy of digital elevation models from the shuttle radar topography mission. *J. Geophys. Res. Earth Surf.* 110 (F2).
- Farley, K.A., 2002. (U-Th)/He dating: Techniques, calibrations, and applications. *Rev. Mineral. Geochem.* 47 (1), 819–844.
- Farley, K.A., Wolf, R.A., Silver, L.T., 1996. The effects of long alpha-stopping distances on (U-Th)/He ages. *Geochim. Cosmochim. Acta* 60 (21), 4223–4229.
- Fink, D., Smith, A., 2007. An inter-comparison of ^{10}Be and ^{26}Al AMS reference standards and the ^{10}Be half-life. *Nucl. Instrum. Methods Phys. Res., Sect. B* 259 (1), 600–609 (Jun.).
- Finnegan, N.J., Schumer, R., Finnegan, S., 2014. A signature of transience in bedrock river incision rates over timescales of 10^3 – 10^7 years. *Nature* 505 (7483), 391–394.
- Fitzgerald, P., Baldwin, S.L., Webb, L., O'Sullivan, P.B., 2006. Interpretation of (U-Th)/He single grain ages from slowly cooled crustal terranes: a case study from the Transantarctic Mountains of southern Victoria Land. *Chem. Geol.* 225 (1), 91–120.
- Flint, J., 1974. Stream gradient as a function of order, magnitude, and discharge. *Water Resour. Res.* 10 (5), 969–973.
- Forte, A.M., Whipple, K.X., Bookhagen, B., Rossi, M.W., 2016. Decoupling of modern shortening rates, climate, and topography in the Caucasus. *Earth Planet. Sci. Lett.* 449, 282–294.
- Galbraith, R., 1981. On statistical models for fission track counts. *Math. Geol.* 13 (6), 471–478.
- Galetzka, J., Melgar, D., Genrich, J.F., Geng, J., Owen, S., Lindsey, E.O., Xu, X., Bock, Y., Avouac, J.-P., Adhikari, L.B., et al., 2015. Slip pulse and resonance of the Kathmandu basin during the 2015 Gorkha earthquake, Nepal. *Science* 349 (6252), 1091–1095.
- Ganti, V., von Hagke, C., Scherler, D., Lamb, M.P., Fischer, W.W., Avouac, J.-P., 2016. Time scale bias in erosion rates of glaciated landscapes. *Sci. Adv.* 2 (10), e1600204.
- Gleadow, A.J.W., Belton, D.X., Kohn, B.O., Brown, R.W., 2002. Fission track dating of phosphate minerals and the thermochronology of apatite. *Rev. Mineral. Geochem.* 48, 579–630.
- Godard, V., Bourlès, D.L., Spinabella, F., Burbank, D.W., Bookhagen, B., Fisher, G.B., Mouline, A., Léanni, L., 2014. Dominance of tectonics over climate in Himalayan denudation. *Geology* 42 (3), 243–246.
- Godard, V., Burbank, D., Bourlès, D., Bookhagen, B., Braucher, R., Fisher, G., 2012. Impact of glacial erosion on ^{10}Be concentrations in fluvial sediments of the Marsyandi catchment, central Nepal. *J. Geophys. Res. Earth Surf.* 117 (F3).
- Godard, V., Burbank, D.W., 2011. Mechanical analysis of controls on strain partitioning in the Himalayas of central Nepal. *J. Geophys. Res. Solid Earth* 116 (B10).
- Granger, D.E., Kirchner, J.W., Finkel, R., 1996. Spatially averaged long-term erosion rates measured from in situ-produced cosmogenic nuclides in alluvial sediment. *J. Geol.* 104, 249–257.
- Guenther, W.R., Reiners, P.W., Ketcham, R.A., Nasdala, L., Giester, G., 2013. Helium diffusion in natural zircon: radiation damage, anisotropy, and the interpretation of zircon (U-Th)/He thermochronology. *Am. J. Sci.* 313 (3), 145–198.
- Hack, J.T., 1957. Studies of longitudinal stream profiles in Virginia and Maryland. U.S. Geol. Surv. Prof. Pap. (294-B), 97.
- Harkins, N., Kirby, E., Heimsath, A., Robinson, R., Reiser, U., 2007. Transient fluvial incision in the headwaters of the Yellow River, northeastern Tibet, China. *J. Geophys. Res.* 112 (F3), 1–21.
- Harvey, J.E., Burbank, D.W., Bookhagen, B., 2015. Along-strike changes in Himalayan thrust geometry: topographic and tectonic discontinuities in western Nepal. *Lithosphere* 7 (5), 511–518.
- Heim, A., Gansser, A., 1939. Central Himalaya: geological observations of the Swiss Expedition 1936. Hindustan Publishing, Delhi.
- Heisinger, B., Lal, D., Jull, A.J.T., Kubik, P.W., Ivy-Ochs, S., Knie, K., Nolte, E., 2002a. Production of selected cosmogenic radionuclides by muons: 2. Capture of negative muons. *Earth Planet. Sci. Lett.* 200 (3–4), 357–369 Jun.
- Heisinger, B., Lal, D., Jull, A.J.T., Kubik, P.W., Ivy-Ochs, S., Neumaier, S., Knie, K., Lazarev, V., Nolte, E., 2002b. Production of selected cosmogenic radionuclides by muons. 1. Fast muons. *Earth Planet. Sci. Lett.* 200 (3–4), 345–355 Jun.
- Herman, F., Copeland, P., Avouac, J.P., Bollinger, L., Mahéo, G., Le Fort, P., Rai, S.S., Foster, D., Pecher, A., Stüwe, K., Henry, P., 2010. Exhumation, crustal deformation, and thermal structure of the Nepal Himalaya derived from the inversion of thermo-chronological and thermobarometric data and modeling of the topography. *J. Geophys. Res.* 115 (B06407).
- Hodges, K., Hurtado, J.M., Whipple, K., 2001. Southward extrusion of Tibetan crust and its effect on Himalayan tectonics. *Tectonics* 20 (6), 799–809.
- Hodges, K., Wobus, C., Ruhl, K., Schildgen, T., Whipple, K., 2004. Quaternary deformation, river steepening, and heavy precipitation at the front of the Higher Himalayan ranges. *Earth Planet. Sci. Lett.* 220, 379–389.
- Hurtrez, J.-E., Sol, C., Lucazeau, F., 1999. Effect of drainage area on hypsometry from an analysis of small-scale drainage basins in the Siwalik Hills (Central Nepal). *Earth Surf. Process. Landf.* 24 (9), 799–808.
- Hyndman, R., Wang, K., 1993. Thermal constraints on the zone of major thrust earthquake failure: the Cascadia subduction zone. *J. Geophys. Res. Solid Earth* 98 (B2), 2039–2060.
- Jade, S., Mukul, M., Gaur, V., Kumar, K., Shrungeshwar, T., Satyal, G., Dumka, R.K., Jagannathan, S., Ananda, M., Kumar, P.D., et al., 2014. Contemporary deformation in the Kashmir-Himachal, Garhwal and Kumaon Himalaya: significant insights from 1995–2008 GPS time series. *J. Geod.* 88 (6), 539–557.
- Kayal, J., Ram, S., Singh, O., Chakraborty, P., Karunakar, G., 2003. Aftershocks of the March 1999 Chamoli earthquake and seismotectonic structure of the Garhwal Himalaya. *Bull. Seismol. Soc. Am.* 93 (1), 109–117.
- Kirby, E., Whipple, K., 2012. Expression of active tectonics in erosional landscapes. *J. Struct. Geol.* 44, 54–75.
- Kohl, C., Nishizumi, K., 1992. Chemical isolation of quartz for measurement of in-situ-produced cosmogenic nuclides. *Geochim. Cosmochim. Acta* 56 (9), 3583–3587.
- Korschinek, G., Bergmaier, A., Faestermann, T., Gerstmann, U.C., Knie, K., Ruegel, G., Wallner, A., Dillmann, I., Dollinger, G., von Gostomski, C.L., Kossert, K., Maiti, M., Poutivtsev, M., Remmert, A., 2010. A new value for the half-life of ^{10}Be by heavy-ion elastic recoil detection and liquid scintillation counting. *Nucl. Instrum. Methods Phys. Res., Sect. B* 268 (2), 187–191 (Jan.).
- Kubik, P.W., Christl, M., Alfmov, V., 2009. New primary Be-10 standard and T1/2 for AMS at ETH. In: Tech. Rep. Jan.
- Kumar, S., Wesnousky, S.G., Rockwell, T.K., Ragona, D., Thakur, V.C., Seitz, G.G., 2001. Earthquake recurrence and rupture dynamics of Himalayan Frontal Thrust, India. *Science* 294 (5550), 2328–2331.
- Lague, D., Hovijs, N., Davy, P., 2005. Discharge, discharge variability, and the bedrock channel profile. *J. Geophys. Res. Earth Surf.* 110 (F4).
- Lal, D., 1991. Cosmic ray labeling of erosion surfaces: in situ nuclide production rates and erosion models. *Earth Planet. Sci. Lett.* 104, 424–439.
- Lavé, J., Avouac, J.-P., 2000. Active folding of fluvial terraces across the Siwaliks Hills, Himalayas of central Nepal. *J. Geophys. Res.* 105 (B3), 5735–5770.
- Lavé, J., Avouac, J.-P., 2001. Fluvial incision and tectonic uplift across the Himalayas of central Nepal. *J. Geophys. Res.* 106 (B11), 26561–26591.
- Lindsey, E.O., Natsukai, R., Xu, X., Shimada, M., Hashimoto, M., Melgar, D., Sandwell, D.T., 2015. Line-of-sight displacement from ALOS-2 interferometry: Mw 7.8 Gorkha earthquake and Mw 7.3 aftershock. *Geophys. Res. Lett.* 42 (16), 6655–6661.
- Ludwig, K., 2012. Isoplot 3.75: A Geochronological Toolkit for Microsoft Excel: Berkeley Geochronology Center Special Publication. 5 (75 pp.).
- Mahesh, P., Rai, S.S., Sivaram, K., Paul, A., Gupta, S., Sarma, R., Gaur, V.K., 2013. One-dimensional reference velocity model and precise locations of earthquake hypocenters in the Kumaon-Garhwal Himalaya. *Bull. Seismol. Soc. Am.* 103 (1), 328–339.
- Mahesh, P., Gupta, S., Saikia, U., Rai, S., 2015. Seismotectonics and crustal stress field in the Kumaon-Garhwal Himalaya. *Tectonophysics* 655, 124–138.
- Mandal, S., Robinson, D., Khanal, S., Das, O., 2015. Redefining the tectonostratigraphic and structural architecture of the Almora klippe and the Ramgarh-Muniarsi thrust sheet in NW India. *Geol. Soc. Lond. Spec. Publ.* 412 (1), 247–269.
- Mandal, S., Robinson, D.M., Kohn, M.J., Khanal, S., Das, O., Bose, S., 2016. Zircon U-Pb ages and Hf isotopes of the Askot klippe, Kumaun, northwest India: implications for Paleoproterozoic tectonics, basin evolution and associated metallogeny of the northern Indian craton margin. *Tectonics* 35 (4), 965–982.
- Moore, M.A., England, P.C., 2001. On the inference of denudation rates from cooling ages of minerals. *Earth Planet. Sci. Lett.* 185 (3), 265–284.
- Morell, K.D., Sandiford, M., Rajendran, C., Rajendran, K., Alimanovic, A., Fink, D., Sanwal, J., 2015. Geomorphology reveals active décollement geometry in the central Himalayan seismic gap. *Lithosphere* 7 (3), 247–256.
- Ni, J., Barazangi, M., 1984. Seismotectonics of the Himalayan collision zone: geometry of the underthrusting Indian plate beneath the Himalaya. *J. Geophys. Res.* 89, 1147–1163.
- Niemi, N., Oskin, M., Burbank, D.W., Heimsath, A., Gabet, E., 2005. Effects of bedrock landslides on cosmogenically determined erosion rates. *Earth Planet. Sci. Lett.* 237, 480–498.
- Nishizumi, K., Imamura, M., Caffee, M.W., Sounthor, J.R., Finkel, R.C., McAninch, J., 2007. Absolute calibration of ^{10}Be AMS standards. *Nucl. Instrum. Methods Phys. Res., Sect. B* 258 (2), 403–413 (May).
- Orme, D.A., Reiners, P.W., Hourigan, J.K., Carrappa, B., 2015. Effects of inherited cores and magmatic overgrowths on zircon (U-Th)/He ages and age-eU trends from Greater Himalayan sequence rocks, Mount Everest region, Tibet. *Geochem. Geophys. Geosyst.* 16 (8), 2499–2507.
- Ouimet, W.B., Whipple, K., Granger, D., 2009. Beyond threshold hillslopes: channel adjustment to base-level fall in tectonically active mountain ranges. *Geology* 37 (9).
- Pandey, M., Tandukar, R.P., Avouac, J.P., Vergne, J., Héritier, T., 1999. Seismotectonics of the Nepal Himalaya from a local seismic network. *J. Asian Earth Sci.* 17 (5–6), 703–712.

- Patel, R., Singh, P., Lal, N., 2015. Thrusting and back-thrusting as post-emplacement kinematics of the Almora klippe: insights from Low-temperature thermochronology. *Tectonophysics* 653, 41–51.
- Patel, R.C., Carter, A., 2009. Exhumation history of the Higher Himalayan Crystalline along Dhauliganga-Gorganga river valleys, NW India: new constraints from fission track analysis. *Tectonics* 28 (TC3004).
- Patel, R.C., Kumar, Y., Lal, N., Kumar, A., 2007. Thermotectonic history of the Chiplakot Crystalline Belt in the Lesser Himalaya, Kumaon, India: constraints from apatite fission-track thermochronology. *J. Asian Earth Sci.* 29, 430–439.
- Perron, J.T., Royden, L., 2013. An integral approach to bedrock river profile analysis. *Earth Surf. Process. Landf.* 38 (6), 570–576.
- Portenga, E., Bierman, P.R., 2011. Understanding Earth's eroding surface with ^{10}Be . *GSA Today* 21 (8).
- Powers, P.M., Lillie, R.J., Yeats, R.S., 1998. Structure and shortening of the Kangra and Dehra Dun reentrants, sub-Himalaya, India. *Geol. Soc. Am. Bull.* 110 (8), 1010–1027.
- Rajendran, C., John, B., Rajendran, K., 2015. Medieval pulse of great earthquakes in the central Himalaya: viewing past activities on the frontal thrust. *J. Geophys. Res. Solid Earth* 120 (3), 1623–1641.
- Rajendran, C.P., Rajendran, K., 2005. The status of central seismic gap: a perspective based on the spatial and temporal aspects of the large Himalayan earthquakes. *Tectonophysics* 395 (19–39).
- Ray, Y., Srivastava, P., 2010. Widespread aggradation in the mountainous catchment of the Alaknanda-Ganga River System: timescales and implications to Hinterland-foreland relationships. *Quat. Sci. Rev.* 29, 2238–2260.
- Reiners, P.W., Brandon, M.T., 2006. Using thermochronology to understand orogenic erosion. *Annu. Rev. Earth Planet. Sci.* 34 (419–466).
- Reiners, P.W., Spell, T.L., Niculescu, S., Zanetti, K.A., 2004. Zircon (U-Th)/He thermochronometry: He diffusion and comparisons with $^{40}\text{Ar}/^{39}\text{Ar}$ dating. *Geochim. Cosmochim. Acta* 68 (8), 1857–1887.
- Robert, X., van der Beek, P., Braun, J., Perry, C., Dubille, M., Mugnier, J.L., 2009. Assessing Quaternary reactivation of the main central thrust zone (central Nepal Himalaya): new thermochronologic data and numerical modeling. *Geology* 37 (8), 731–734.
- Safran, E.B., Bierman, P.R., Aalto, R., Dunne, T., Whipple, K.X., Caffee, M., 2005. Erosion rates driven by channel network incision in the Bolivian Andes. *Earth Surf. Process. Landf.* 30, 1007–1024.
- Schaller, M., von Blanckenburg, F., Hovius, N., Kubik, P.W., 2001. Large-scale erosion rates from in-situ-produced cosmogenic nuclides in European river sediments. *Earth Planet. Sci. Lett.* 188 (3–4), 441–458.
- Scherler, D., Bookhagen, B., Strecker, M.R., 2014. Tectonic control on ^{10}Be -derived erosion rates in the Garhwal Himalaya, India. *J. Geophys. Res. Earth Surf.* 119 (2), 83–105 Feb.
- Scherler, D., Bookhagen, B., Wulf, H., Preusser, F., Strecker, M.R., 2015. Increased late Pleistocene erosion rates during fluvial aggradation in the Garhwal Himalaya, northern India. *Earth Planet. Sci. Lett.* 428, 255–266.
- Schwanhart, W., Scherler, D., 2014. Short communication: Topotoolbox 2-matlab-based software for topographic analysis and modeling in earth surface sciences. *Earth Surf. Dyn.* 2 (1), 1.
- Seeber, L., Gornitz, V., 1983. River profiles along the Himalayan arc as indicators of active tectonics. *Tectonophysics* 92 (4), 335–367.
- Singh, P., Patel, R.C., Lal, N., 2012. Plio-Pleistocene in-sequence thrust propagation along the main central thrust zone (Kumaon-Garhwal Himalaya, India): new thermochronological data. *Tectonophysics* 574–575, 193–203.
- Snyder, N.P., Whipple, K.X., Tucker, G.E., Merritts, D.J., 2000. Landscape response to tectonic forcing: DEM analysis of stream profiles in the Mendocino triple junction region, northern California. *Geol. Soc. Am. Bull.* 112, 1250–1263.
- Sorkhabi, R.B., Stump, E., Foland, K.A., Jain, A.K., 1996. Fission-track and $^{40}\text{Ar}/^{39}\text{Ar}$ evidence for episodic denudation of the Gangotri granites in the Garhwal Higher Himalaya, India. *Tectonophysics* 260 (1), 187–199.
- Srivastava, P., Mitra, G., 1994. Thrust geometries and deep structure of the outer and Lesser Himalaya, Kumaon and Garhwal (India): implications for evolution of the Himalayan fold-and-thrust belt. *Tectonics* 13 (1), 89–109.
- Srivastava, P., Tripathi, J., Islam, R., Jaiswal, M., 2008. Fashion and phases of late Pleistocene aggradation and incision in Alaknanda River Valley, western Himalaya, India. *Quatern. Res.* 70, 68–80.
- Stevens, V., Avouac, J., 2015. Interseismic coupling on the main Himalayan thrust. *Geophys. Res. Lett.* 42 (14), 5828–5837.
- Thiede, R., Ehlers, T.A., 2013. Large spatial and temporal variations in Himalayan denudation. *Earth Planet. Sci. Lett.* 371–372, 278–293.
- Thiede, R., Ehlers, T.A., Bookhagen, B., Strecker, M., 2009. Erosional variability along the northwest Himalaya. *J. Geophys. Res.* 114 (F01015), 1–19.
- Valdiya, K.S., 1980. Geology of Kumaun Lesser Himalaya Interim Record. Wadia Institute of Himalayan Geology, Dehradun.
- van der Beek, P., Litty, C., Baudin, M., Mercier, J., Robert, X., Hardwick, E., 2016. Contrasting tectonically driven exhumation and incision patterns, western versus central Nepal Himalaya. *Geology* 44 (4), 327–330.
- Vance, D., Bickle, M., Ivy-Ochs, S., Kubik, P.W., 2003. Erosion and exhumation in the Himalaya from cosmogenic isotope inventories of river sediments. *Earth Planet. Sci. Lett.* 206, 273–288.
- von Blanckenburg, F., 2005. The control mechanisms of erosion and weathering at basin scale from cosmogenic nuclides in river sediment. *Earth Planet. Sci. Lett.* 242, 224–239.
- von Blanckenburg, F., Belshaw, N.S., O'Nions, R.K., 1996. Separation of ^{9}Be and cosmogenic ^{10}Be from environmental materials and SIMS isotope dilution analysis. *Chem. Geol.* 129 (1), 93–99.
- Wang, K., Fialko, Y., 2015. Slip model of the 2015 Mw 7.8 Gorkha (Nepal) earthquake from inversions of ALOS-2 and GPS data. *Geophys. Res. Lett.* 42 (18), 7452–7458.
- Webb, A.A.G., Yin, A., Harrison, T.M., Célérier, J., Gehrels, G., Manning, C., Grove, M., 2011. Cenozoic tectonic history of the Himachal Himalaya (northwestern India) and its constraints on the formation mechanism of the Himalayan orogen. *Geosphere* 7 (4), 1013–1061.
- Wesnousky, S.G., Kumar, S., Mohindra, R., Thakur, V., 1999. Uplift and convergence along the himalayan frontal thrust of india. *Tectonics* 18 (6), 967–976.
- Whipp, D.M., Ehlers, T.A., Blythe, A.E., Huntington, K.W., Hodges, K.V., Burbank, D.W., 2007. Plio-quaternary exhumation history of the central Nepalese Himalaya: 2. Thermokinematic and thermochronometer age prediction model. *Tectonics* 26 (3).
- Whipple, K.X., Shirzaei, M., Hodges, K.V., Arrowsmith, J.R., 2016. Active shortening within the Himalayan orogenic wedge implied by the 2015 Gorkha earthquake. *Nat. Geosci.* 9, 711–716.
- Whipple, K.X., Tucker, G.T., 1999. Dynamics of the stream-power river incision model: implications for height limits of mountain ranges, landscape response timescales, and research needs. *J. Geophys. Res.* 104 (B8), 17661–17674.
- Wildman, M., Brown, R., Beucher, R., Persano, C., Stuart, F., Gallagher, K., Schwanthal, J., Carter, A., 2016. The chronology and tectonic style of landscape evolution along the elevated Atlantic continental margin of South Africa resolved by joint apatite fission track and (U-Th-Sm)/He thermochronology. *Tectonics* 35, 511–545.
- Willenbring, J.K., Codilean, A.T., McElroy, B., 2013. Earth is (mostly) flat: apportionment of the flux of continental sediment over millennial time scales. *Geology* 41 (3), 343–346.
- Willett, S.D., Brandon, M.T., 2002. On steady states in mountain belts. *Geology* 30 (2), 175–178.
- Willett, S.D., Brandon, M.T., 2013. Some analytical methods for converting thermochronometric age to erosion rate. *Geochem. Geophys. Geosyst.* 14 (1), 209–222.
- Wobus, C., Heimsath, A., Whipple, K., Hodges, K., 2005. Active out-of-sequence thrust faulting in the central Nepalese Himalaya. *Nature* 434, 1008–1011.
- Wobus, C., Hodges, K., Whipple, K., 2003. Has focused denudation sustained active thrusting at the Himalayan topographic front? *Geology* 31 (10), 861–864.
- Wobus, C., Whipple, K., Hodges, K., 2006a. Neotectonics of the central Nepalese himalaya: constraints from geomorphology, detrital $^{40}\text{Ar}/^{39}\text{Ar}$ thermochronology, and thermal modeling. *Tectonics* 25 (4).
- Wobus, C., Whipple, K., Kirby, E., Snyder, N., Johnson, J., Spyropoulos, K., Crosby, B., Sheehan, D., 2006b. Tectonics from topography: procedures, promise, and pitfalls. In: Willett, S.D., Hovius, N., Brandon, M.T., Fisher, D.M. (Eds.), *Tectonics, Climate, and Landscape Evolution: Geological Society of America Special Paper* 398, Penrose Conference Series. Geol. Soc. Am.. pp. 55–74.